A Cost-Effective Segmented Dynamic Wireless Charging System With Stable Efficiency and Output Power

Changsong Cai, *Member, IEEE*, Maryam Saeedifard, *Fellow, IEEE*, Junhua Wang, *Member, IEEE*, Pengcheng Zhang, *Member, IEEE*, Jiansong Zhao, and Yunshan Hong

***Abstract*—This article presents a cost-effective dynamic wireless power transfer (DWPT) system for efficient and stable output power charging of autonomous moving equipment. The proposed system is realized based on a low-cost segmented configuration and a flexible operating strategy. Specifically, the configuration is a combination of a dynamic *T*-series/series topology and extended transmitter (Tx) coils. The topology eliminates the cross-coupling impact of adjacent Tx coils and tunes the dynamic circuits at resonance. It makes the switching circuits equivalent to a unified analytical model for simplified control, which reduces the cost of inverter, decoupling, compensation, and position detection in the DWPT. The extended Tx coil with a simplified structure, which is obtained from winding coupling characteristics and a finite-element analysis based algorithm, is proposed to improve the moving misalignment tolerance, thereby reducing the number of Tx segments. An operating principle with three modes behind the proposed strategy is designed to fully utilize the efficient coupling area of individual Tx segment and improve the efficiency in the transition region from one segment to the other one. The operating parameters including the transition and compensation are obtained based on the topology and its operating principles. Position detection and power regulation methods are developed and embedded in the system control to configure/coordinate the segmented coils as the strategy and mitigate power fluctuation in the transition region. The performance and effectiveness of the proposed cost-effective DWPT system are evaluated based on experimental results on a scaled-down prototype.**

***Index Terms*—Autonomous moving equipment, cost-effective, dynamic wireless power transfer (DWPT), extended transmitter (Tx) segments, *T*-series/series compensation topology.**

I. Introduction

Over the past decade, wireless power transfer (WPT) technology in the form of stationary and dynamic charging has become the focus of research for electric mobility [1]–[3]. Dynamic wireless power transfer (DWPT) in an automatic operation route can potentially improve the working efficiency of autonomous moving equipment, such as inspection robots in substations and intelligent-guided vehicles in warehouses. As the motion of these types of equipment is relatively slow, the DWPT is promising and effective [4], [5].

In terms of the transmitter (Tx) type, the DWPT is divided into two major categories: 1) long-track Tx-based DWPT [2], [6], [7], and 2) segmented Tx-based DWPT [8]–[20]. In the former, multiple receivers (Rxs) can be charged simultaneously and are implemented based on a simple circuit and coil structure. Yet, the long returning path loop with tens of times the radius of Rx coil inevitably suffers from a relatively large equivalent series resistance (ESR) and is poorly coupled to the Rx coil, which results in a low efficiency [6]–[15]. Meanwhile, significant leakage magnetic field would result in a high electromagnetic interference (EMI). In the latter, the Tx coils are arranged in the moving route to power the Rx. The controllable and switchable coils are turned ON and OFF according to the position of Rx [8]–[10], [12]–[20]. As opposed to the long-track Tx, the segmented Tx achieves a higher efficiency and a lower EMI. Besides, the segmented coils are usually designed to be identical, which makes the construction of the Tx modular/scalable.

Despite the aforementioned advantages of the segmented DWPT, there are several technical challenges for practical applications. One is the high manufacturing cost compared with the long-track Tx one, which is due to the large number of power and compensation components used in the segmented design. Another challenge is the performance stability of the dynamic charging in terms of efficiency and output power.

Conventionally, a relatively large distance between the adjacent Tx coils is set to eliminate the cross coupling so that the Tx coils are decoupled and control and implementation become simple [8]–[10]. However, this would ironically cause the in-motion efficiency and output power to fluctuate. A segmented system without any active switch is designed in [11] to reduce the cost by controlling the power flow of Tx coils with the impedance of each Tx coil loop. The impedance variation is caused by

---

Manuscript received July 6, 2021; revised September 26, 2021 and December 9, 2021; accepted January 6, 2022. Date of publication January 14, 2022; date of current version March 24, 2022. This work was supported in part by the China Postdoctoral Science Foundation under Projects 2021M692466 and 2021TQ0249 and in part by the Science and Technology Project of State Grid Corporation of China under Project 5200-201916252A. Recommended for publication by Associate Editor A. Safaee. *(Corresponding author: Junhua Wang.)*

Changsong Cai, Junhua Wang, Jiansong Zhao, and Yunshan Hong are with the School of Electrical Engineering and Automation, Wuhan University, Wuhan 430072, China (e-mail: changsongcai@whu.edu.cn; junhuawang@whu.edu.cn; jasonzhao@whu.edu.cn; hyszwd@whu.edu.cn).

Maryam Saeedifard is with the School of Electrical and Computer Engineering, Georgia Institute of Technology, Atlanta, GA 30332 USA (e-mail: maryam@ece.gatech.edu).

Pengcheng Zhang is with the Department of Electrical Engineering, Tsinghua University, Beijing 100084, China (e-mail: pczhang@mail.tsinghua.edu.cn).

Color versions of one or more figures in this article are available at https://doi.org/10.1109/TPEL.2022.3143128.

Digital Object Identifier 10.1109/TPEL.2022.3143128

the larger ferrite core of moving Rx, which is not suitable for compact Rx applications. All the Tx coils are activated wherever the Rx locates, which makes the system sensitive to external interference. Moreover, the in-motion efficiency and output power fluctuate.

In the technical literature, a number of strategies have been proposed/investigated to restrain the output power fluctuation of DWPT systems. One common method is to redesign the structure of the Tx and Rx coils. Several adjacent Tx coils are activated simultaneously to enforce stable couplings between the Tx coil array and the Rx coil [12]–[16]. Two Tx coils in [12], four Tx coils in [13], six Tx coils in [14], seven Tx coils in [15], and five Tx coils in [16] are designed to provide stable couplings when the Rx moves in the area covered by those Tx coils. The distance between the Tx coils in [12] and [13] is regulated to form a relatively stable mutual inductance (MI) with the Rx coil. By optimizing the size or number of turns of the Rx coil, the MI between the Tx and Rx coils is stabilized in [14] and [15]. However, the multiple segmented Tx coils with similar size of Rx coil in [12]–[16] produce a limited charging range, which demands more Tx coils to provide the required charging length. To offset the cost, multiple Tx coil loops can be connected in parallel to share one inverter [14]. Yet, the use of compensation components for each Tx coil still imposes a high cost. Moreover, when the generated fields of Tx coils are in opposite directions, their magnetic fluxes are counteracted, thereby deteriorating/loosening the coupling. The interacted fluxes also induce cross couplings among Tx coils with their adverse impacts, which degrade the system performance [12], [13] and make the tuning design complicated [14]. The Tx coils in [15] and [16] are refined to eliminate the cross coupling between the adjacent Tx coils. Yet, the adjacent unipolar and bipolar Tx coils [15] and bipolar cross-coupling inductors [16], which are to eliminate cross coupling, make the system expensive.

To minimize the power pulsation, a switching strategy of adjacent Tx coils based on decoupling characteristics is proposed in [17]. However, the efficiency decreases when the Rx locates in the transition region between the Tx coils. A compensation network, consisting of three elements in each activated Tx coil and a series capacitor in the Rx side, is designed to cooperate with dual Tx coils to restrain the power fluctuation under varying coupling [18]. The compensation parameters for minimizing the fluctuation do not make the system operate in a resonant state, and zero phase angle (ZPA) input characteristic is lost. Accordingly, the VA rating and power losses are increased, and a high level of coupling is required to make the system efficient. A switching control based DWPT system with equivalent series Tx coils is presented in [19]. However, an additional capacitor matrix along with switching control is needed to tune the varying impedances caused by cross coupling. Moreover, the topology would lead to high voltage stress on switches. An expandable N-legged converter topology to drive segmented Tx coils with the objective of reducing inverter cost is presented in [20]. The Tx coils are positioned closely to stabilize the output power, and additional coupled inductors are designed to eliminate the impacts of cross coupling. The systems in [19] and [20] employing Tx coils with similar size of Rx coil demand more Tx coils for the required charging area. Additionally, the output power with one operating Tx coil fluctuates relatively violently, and the efficiency decreases when Rx locates in the area with multiple activated Tx coils.

Consequently, to reduce the number and cost of segmented Tx coils while enabling stable and efficient operation, there is a need for a cost-effective approach to stabilize the performance and eliminate the cross coupling impact of the DWPT systems.

Position detection of dynamic Rx is the foundation for switching the segmented Tx coils, which was missed in most of the prior work [12]–[15], [17], [18], [20]. Although radio-frequency identification and ultrasound/optic sensors can be employed for coil positioning, they might be affected by the magnetic field of the DWPT system, which then necessitates additional hardware [19]. To determine the position of the Rx coil, MI detection-based positioning methods for stationary WPT have been investigated [2], [21]. For DWPT, an MI detection-based method to detect the center coil of five Tx coils in [16] and multiple excitations in [22] are proposed. However, the single-point current sensing-based position detection in [16] is sensitive and needs to work with multiple operating Tx coils, simultaneously. The cost and complexity of the method in [22] are high because of the significant numbers of inverters and sensors. In summary, a low-cost and precise position detection method for the control of the DWPT systems should be studied.

When it comes to the DWPT of autonomous moving equipment, in addition to the aforementioned technical issues, the size of the Rx coil to be installed is limited because of the restricted space [5], [10]. Meanwhile, not only the coupling along the moving direction but also the lateral misalignment caused by unmanned errors should be taken into consideration. In [23]–[26], asymmetrical unipolar coils have been designed with multidirectional stable MIs. Unipolar Tx coils, which produce a uniform vertical flux by properly designing their turn spaces or direction of windings, can serve as a modular single Tx coil of segmented DWPT systems. However, the multithread windings with different turn spaces in [23], [24], and [26] and different directions in [25] make the coupling coil design and implementation complicated.

To achieve a cost-effective, performance-stabilized DWPT system and fit it well into the application of autonomous moving equipment, a low-cost segmented configuration and its associated operating strategy are proposed and investigated in this article. The configuration is mainly comprised of a dynamic *T*-series/series topology and extended Tx segments. The novel topology eliminates the cross-coupling impact of the adjacent Tx coils and tunes the circuits under different operating modes at resonance with ZPA input and load-independent output. In addition, it makes the switching circuits equivalent to a unified analytical model for simplified control, which reduces the cost of inverter, decoupling, compensation, and position detection. The individual Tx coil segment is extended with a simplified structure for an enlarged stable and efficient coupling area considering moving and lateral misalignments of Rx and is obtained by a finite-element analysis (FEA) based algorithm. The operating strategy with three modes fully utilizes the coupling

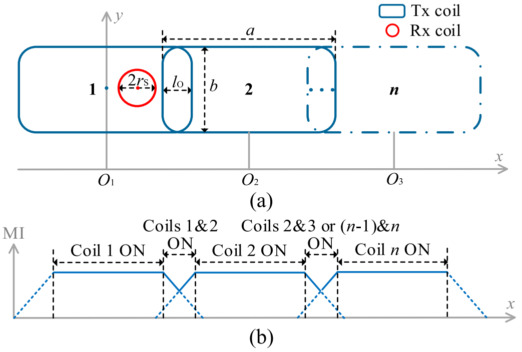

Fig. 1. Proposed DWPT system based on segmented Tx coils. (a) Layout of the coils. (b) Operating strategy.

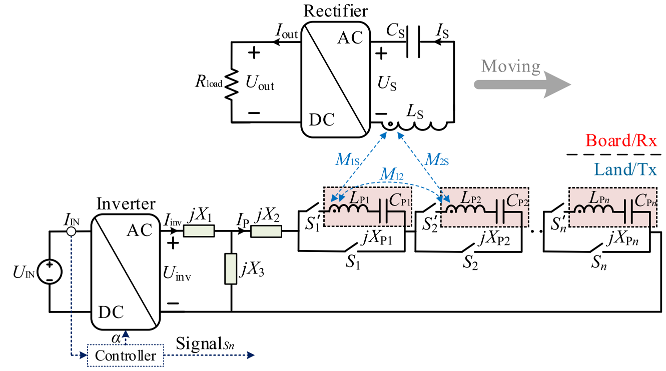

Fig. 2. Schematic diagram of the proposed DWPT system.

TABLE I
SYMBOLS AND MEANINGS IN THE TOPOLOGY DIAGRAM AND CIRCUITS

Symbol	Meaning
U_{IN} and I_{IN}	DC input voltage and current
U_{inv} and I_{inv}	Output voltage and current of the inverter
X_1, X_2 and X_3	Components of the T circuit topology
I_{P}	Current in the Tx coil circuit
$L_{\mathrm{P}n}$	Self-inductance of the nth Tx coil
$C_{\mathrm{P}n}$	Compensation capacitor in the circuit of the nth Tx
S_n and S_n'	Switches in the circuit of the nth Tx coil
$M_{n(n+1)}$	Cross MI between the nth and $(n+1)$th Tx coils
$M_{\mathrm{P}n\mathrm{S}}$	MI between the nth Tx coil and Rx coil
U_{S} and I_{S}	Rx output voltage and current
L_{S} and C_{S}	Self-inductance and compensation capacitor of Rx coil
R_{load}	Equivalent resistance of the load
U_{out} and I_{out}	DC output voltage and current of the system
α	Phase-shifting angle of the inverter
$X_{\mathrm{P}i}$ (i=1, 2, e)	Equivalent reactance of the Tx coil loop in Fig. 3
$X_{\mathrm{S}i}$ (i=1, 2, e)	Equivalent reactance of the Rx coil loop in Fig. 3
$L_{\mathrm{P}i}$ (i=1, 2, e)	Equivalent self-inductance of the Tx coil loop in Fig. 3
$C_{\mathrm{P}i}$ (i=1, 2, e)	Compensation capacitor of the Tx coil loop in Fig. 3
$M_{\mathrm{PS}i}$ (i=1, 2, e)	Equivalent MI between Tx and Rx coil loops in Fig. 3

area of the designed Tx coil and stabilizes the efficiency and output power in all operating stages. A dynamic position factor based on the unified analytical model is employed to avoid the impact of the symmetrical coupling profile and detect the current and upcoming region of Rx coil during moving and charging. The corresponding system control with an embedded position detection in transition mode and power regulation is developed to configure/coordinate the Tx coils only by monitoring a single dc input current. The performance of the system is evaluated based on results obtained from an experimental prototype. The proposed design with a lower construction cost stabilizes the dynamic charging performance in all stages, which not only mitigates the power fluctuations but also improves the efficiency.

The rest of this article is organized as follows. Section II presents an overview of the proposed DWPT system along with its basics of operation. In Section III, a simplified and extended Tx coil design in combination with its segmented operation and compensation sensitivity analysis are elaborated. Section IV embeds position detection and power regulation capabilities in the proposed system control. Experimental results and comparison with the state-of-the-art are presented in Section V. Finally, Section VI concludes this article.

II. SYSTEM OVERVIEW AND BASICS OF OPERATION

A. *Overview of the Proposed DWPT System*

The layout of the proposed segmented DWPT system along with its operating strategy is presented in Fig. 1. The Tx side is comprised of n identical Tx coil segments, which are meant to provide an enlarged stable coupling area for the compact Rx, as shown in Fig. 1(a). The basics of operating strategy and coordination among the segmented Tx coils are depicted in Fig. 1(b). Taking coils 1 and 2 as the analysis example, there are three modes of operation as the Rx moves along the x-axis. In mode A, coil 1 is activated when the Rx locates in the stable coupling area of coil 1. In mode B, coils 1 and 2 are activated simultaneously to maintain the transmission efficiency when Rx locates in the transition region between the two adjacent coils. In mode C, coil 2 is activated when the Rx locates in the stable coupling area of coil 2. As highlighted in Fig. 1(b), the normal operation of coil 1 and the transition from coil 1 to 2 can be regarded as one operation cycle of the DWPT scheme. Over the whole charging length, as the Rx sweeps the Tx coil segments, there are n cycles, which can be similarly analyzed.

The main distinction between the proposed DWPT scheme and prior work in the literature is that, in the proposed system, the adjacent coils are arranged and coordinated to stabilize the transmission performance in all stages. Meanwhile, the available stable charging length can be realized by fewer Tx coil segments. This is opposed to the existing work where the output power fluctuation is suppressed by either the decoupled or MI-superposed Tx coils.

The schematic circuit diagram of the proposed dynamic charging system is detailed in Fig. 2, with the defined symbols listed in Table I. A full-bridge inverter is employed to power the Tx loop. The segmented Tx coil circuit is modeled by n identical series-connected circuits. The circuit of each Tx coil segment is comprised of a coil segment with the inductance of $L_{\mathrm{P}n}$, a compensation capacitor with the capacitance of $C_{\mathrm{P}n}$, and a pair of complementary switches S_n and S_n'. Each coil segment is connected in series with the capacitor $C_{\mathrm{P}n}$ to reduce the voltage stress on nonconducting switches and compensate the inductance differences caused by connection wires and manufacturing. The complementary switches are to activate or deactivate each corresponding coil segment, i.e., coil n is activated when S_n' is ON and S_n is OFF and deactivated when S_n' is OFF and S_n is ON. A relay or a bidirectional switch with two inverse series-connected MOSFETs can serve as the switch in the segmented DWPT system [10], [27]. Based on the relatively slow-moving charging and switching characteristics of autonomous equipment, photocoupler-based relays with normally opened and closed contactors are employed to serve as the switches S_n and S_n' to halve the number of switches or relays required for this design. Since at any instant, at most two Tx coil segments are activated, the equivalent inductance of the coils in series is not substantial, and consequently, does not cause any instability in the resonant circuit.

The *T* circuit components, i.e., X_1, X_2, and X_3, are embedded in the Tx to eliminate the impacts of cross MI and achieve ZPA input and load-independent I_{P} under different operating modes. The *T* components work with different activated coils, which reduce the use of compensation components. Moreover, the series Tx coil loop makes the system with dynamic circuits equivalent to a one-to-one magnetic coupled system as the unified analytical model. Thus, only one channel sampling is required in the Tx with the topology, and the corresponding control is accordingly simplified. The Rx coil and capacitor C_{S} are in series to obtain a load-independent output voltage. The proposed topology is called the *T*-series/series compensation topology, which is elaborated in Section II-B. Compared with the previously reported stable coupling solutions with several activated Tx coils, the proposed system is controlled flexibly and implemented cost-effectively with fewer number of power and compensation components. In addition, the impacts of the cross coupling between the adjacent Tx coil segments are restrained in a low-cost manner. Meanwhile, the performance in terms of efficiency and output power is stabilized.

B. Analysis and Design of the Compensation Topology

Assuming that all n Tx coil circuits have identical parameters, the segmented operating strategy has three modes within each cycle formed by two adjacent coil segments, as highlighted in Fig. 1(b). The equivalent circuits of the DWPT system in the three modes, i.e., modes A, B, and C are presented. The definitions of the remaining symbols are provided in Table I.

The loop voltage equation of the circuits in Fig. 3(a) and (c) can be expressed by (1), where $X_{\mathrm{S}} = \omega L_{\mathrm{S}} – 1/(\omega C_{\mathrm{S}})$, $X_{\mathrm{P1}} = \omega L_{\mathrm{P1}} – 1/(\omega C_{\mathrm{P1}})$, and $X_{\mathrm{P2}} = \omega L_{\mathrm{P2}} – 1/(\omega C_{\mathrm{P2}})$. R_{L} is the equivalent load before the rectifier and $R_{\mathrm{L}} = 8R_{\mathrm{load}}/\pi^2$. The loop voltage equation of the circuit in Fig. 3(b) is expressed by (2).

TABLE II
LIST OF VARIABLES IN FIG. 3

Mode	Variable				
	X_{Pe}	X_{Se}	L_{Pe}	M_{PSe}	C_{Pe}
A	X_{P1}	X_{S}	L_{P1}	M_{P1S}	C_{P1}
B	$X_{\mathrm{P1}}+X_{\mathrm{P2}}+2\omega M_{12}$	X_{S}	$L_{\mathrm{P1}}+L_{\mathrm{P2}}+2M_{12}$	$M_{\mathrm{P2S}}+M_{\mathrm{P1S}}$	$\dfrac{C_{\mathrm{P1}}C_{\mathrm{P2}}}{C_{\mathrm{P1}}+C_{\mathrm{P2}}}$
C	X_{P2}	X_{S}	L_{P2}	M_{P2S}	C_{P2}

By substituting for $X_{\mathrm{Pe}} = X_{\mathrm{P1}}+X_{\mathrm{P2}}+2j\omega M_{12}$ and $\omega M_{\mathrm{Se}} = M_{\mathrm{P1S}}+M_{\mathrm{P2S}}$, (2) can be simplified as

$$\begin{bmatrix} U_{\mathrm{inv}} \\ 0 \\ 0 \end{bmatrix} = \begin{bmatrix} jX_1 + jX_3 & -jX_3 & 0 \\ -jX_3 & jX_2 + jX_3 + jX_{\mathrm{Pe}} & j\omega M_{\mathrm{Se}} \\ 0 & j\omega M_{\mathrm{Se}} & jX_{\mathrm{S}} + R_{\mathrm{L}} \end{bmatrix} \times \begin{bmatrix} I_{\mathrm{inv}} \\ I_{\mathrm{P}} \\ I_{\mathrm{S}} \end{bmatrix}. \tag{3}$$

Subsequently, the equivalent circuits in the three operation modes can be represented by the general analytical circuit in Fig. 3(d), whose variables are listed in Table II.

To guarantee ZPA input and load-independent output voltage characteristics and to ensure constant I_{P} in different modes, the following must hold [28]:

$$X_1 + X_3 = 0 \tag{4a}$$

$$X_2 + X_3 + X_{\mathrm{Pe}} = 0 \tag{4b}$$

$$X_{\mathrm{Se}} = 0. \tag{4c}$$

Subsequently, I_{S} can be deduced from the loop voltage equation. Accordingly, U_{S} can be obtained and the voltage gain is expressed as

$$G_{\mathrm{UU}} = \frac{U_{\mathrm{S}}}{U_{\mathrm{inv}}} = \frac{\omega M_{\mathrm{Se}}}{X_3} \tag{5}$$

which is load-independent. Thus, X_3 can be designed to regulate the gain according to the output requirements. Once X_3 is determined, X_1 can be calculated based on (4a). Since L_{S} does not change within the three modes, (4c) can be easily met by adjusting C_{S}. Equation (4b) under the three modes is expressed by

$$\begin{cases} X_2 + X_3 + X_{\mathrm{P1}} = 0 & \text{(Mode A)} \\ X_2 + X_3 + X_{\mathrm{P1}} + X_{\mathrm{P2}} + 2\omega M_{12} = 0 & \text{(Mode B)} \\ X_2 + X_3 + X_{\mathrm{P2}} = 0 & \text{(Mode C).} \end{cases} \tag{6}$$

$$\begin{bmatrix} U_{\mathrm{inv}} \\ 0 \\ 0 \end{bmatrix} = \begin{bmatrix} jX_1 + jX_3 & -jX_3 & 0 \\ -jX_3 & jX_2 + jX_{\mathrm{XP1(XP2)}} + jX_3 & j\omega M_{\mathrm{P1S(P2S)}} \\ 0 & j\omega M_{\mathrm{P1S(P2S)}} & jX_{\mathrm{S}} + R_{\mathrm{L}} \end{bmatrix} \begin{bmatrix} I_{\mathrm{inv}} \\ I_{\mathrm{P}} \\ I_{\mathrm{S}} \end{bmatrix} \tag{1}$$

$$\begin{bmatrix} U_{\mathrm{inv}} \\ 0 \\ 0 \end{bmatrix} = \begin{bmatrix} jX_1 + jX_3 & -jX_3 & 0 \\ -jX_3 & jX_2 + jX_3 + jX_{\mathrm{XP1}} + jX_{\mathrm{XP2}} + 2j\omega M_{12} & j\omega\left(M_{\mathrm{P1S}} + M_{\mathrm{P2S}}\right) \\ 0 & j\omega\left(M_{\mathrm{P1S}} + M_{\mathrm{P2S}}\right) & jX_{\mathrm{S}} + R_{\mathrm{L}} \end{bmatrix} \begin{bmatrix} I_{\mathrm{inv}} \\ I_{\mathrm{P}} \\ I_{\mathrm{S}} \end{bmatrix} \tag{2}$$

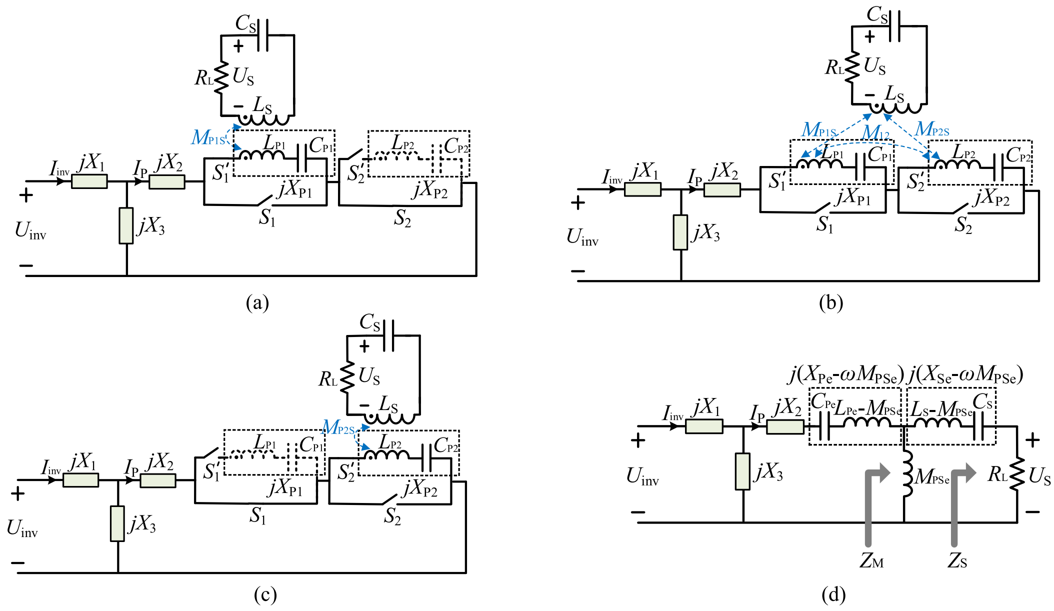

Fig. 3. Equivalent circuits of the three operation modes in the designed DWPT system. (a) Mode A: Prior Tx coil 1 operating. (b) Mode B: Adjacent coils 1 and 2 operating simultaneously. (c) Mode C: Tx coil 2 operating. (d) Analytical equivalent circuit of the proposed topology.

By assuming that $L_{P1} = L_{P2} = L_P$ and $C_{P1} = C_{P2} = C_P$, which translate to $X_{P1} = X_{P2} = X_P$, (6) is simplified to

$$\begin{cases} X_2 + X_3 + X_P = 0 \\ X_P + 2\omega M_{12} = 0. \end{cases} \tag{7}$$

Therefore, X_2 and C_P can be obtained by

$$X_2 = -X_3 + 2\omega M_{12} \tag{8a}$$

$$C_P = \frac{1}{\omega^2 \left(L_P + 2M_{12}\right)}. \tag{8b}$$

Based on the aforementioned analysis, the proposed DWPT topology eliminates the impacts of cross coupling and guarantees ZPA input and load-independent output characteristics under different modes. Moreover, based on the deduced parameters in (4), the equivalent circuit of different modes can be represented by the model of Fig. 3(d) and solely based on variable M_{PSe}, which simplifies the modeling process.

C. Performances Analysis Under Different Modes

In the proposed system, efficiency and output power are two important transmission performance metrics that need to be considered in the design process. Based on the analytical circuit of Fig. 3(d), the transmission efficiency considering power losses on the coil loops is expressed by

$$\begin{aligned} \eta &= \frac{\mathrm{re}(Z_M)}{\mathrm{re}(Z_M) + R_{Lpe}} \cdot \frac{\mathrm{re}(Z_S)}{\mathrm{re}(Z_S) + R_{Ls}} \\ &= \frac{\omega^2 {M_{Se}}^2}{\omega^2 {M_{Se}}^2 + R_{Lpe}\left(R_L + R_{Ls}\right)} \cdot \frac{R_L}{R_L + R_{Ls}} \end{aligned} \tag{9}$$

where R_{Lpe} and R_{Ls} are the ESRs of Tx and Rx coil loops, respectively. The efficiency in (9) can be expressed as follows:

$$\eta = \frac{{k_{PSe}}^2 Q_{Lpe} Q_{Ls} Q_{Lpe} Q_L}{\left({k_{PSe}}^2 Q_{Lpe} Q_{Ls} Q_L + Q_{Lpe} + Q_L\right) \cdot \left(Q_{Ls} + Q_L\right)} \tag{10a}$$

$$k_{PSe} = \frac{M_{PSe}}{\sqrt{L_{Pe} L_S}} \tag{10b}$$

where $Q_{Lpe} = \omega L_{Pe}/2R_{Lpe}$, $Q_{Ls} = \omega L_S/R_{Ls}$, and $Q_L = \omega L_S/R_L$. By solving $\mathrm{d}\eta/\mathrm{d}Q_L = 0$, the transmission efficiency with an optimized load can be attained by

$$\eta = \frac{{k_{PSe}}^2 Q_{Lpe} Q_{Ls}}{\left(\sqrt{{k_{PSe}}^2 Q_{Lpe} Q_{Ls} + 1} + 1\right)^2}. \tag{11}$$

The output power of the DWPT system can be deduced by

$$P_{out} = {G_{UU}}^2 \cdot \frac{{U_{inv}}^2}{R_L}. \tag{12}$$

Setting $\tau = {k_{PSe}}^2 Q_{Lpe} Q_{Ls}$, the efficiency in (11) rises as τ increases. Fig. 4 shows τ^* and ${G_{UU}}^*$ versus M^*, and η^* versus τ for various values of M^*. Subscript "*" represents the normalized value of the corresponding parameter, meaning that $\tau^* = \tau_e/\tau_r$, $M^* = M_{PSe}/M_{PSr}$, ${G_{UU}}^* = G_{UUe}/G_{UUr}$, and $\eta^* = \eta_e/\eta_r$. With one activated Tx coil in modes A and C, subscripts "e" and "r" refer to the corresponding value produced by one Tx coil segment and its reference value, respectively. With dual activated Tx coils in mode B, subscripts "e" and "r" refer to the value produced by dual Tx coils and the designed stable value produced by one Tx coil, respectively.

In Fig. 4(a), τ increases with the increase of the MI, whereas G_{UU} is proportional to the MI. This, in modes A and C, means that the MIs, M_{P1S} or M_{P2S} should be stable and efficient to

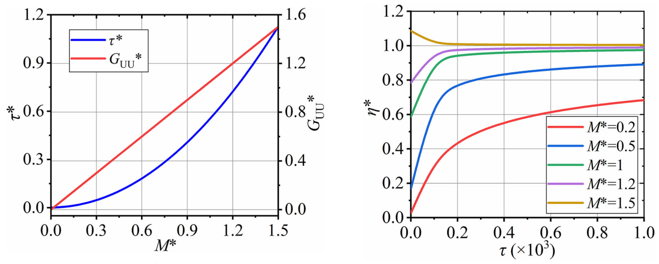

(a) (b)

Fig. 4. (a) τ^* and $G_{\mathrm{UU}}{}^*$ versus M^*. (b) η^* versus τ under different values of M^*.

TABLE III
SYMBOLS AND MEANINGS OF THE PROPOSED COILS

Symbol	Meaning
h	Airgap distance
a and b	Length and width of the Px winding
c and d	Length and width of the Cx winding
w_{Px} (w_{a}=w_{b})	Width of the Px winding
w_{Cx} (w_{c}=w_{d})	Width of the Cx winding
N_{Px} and N_{Cx}	Numbers of turns of the two Tx windings
r_{S}	Radius of Rx coil
w_{S}	Width of Rx coil
N_{S}	Number of turns of Rx coil
t_{W}	Thickness of wires
t_{f}	Thickness of ferrites
t_{S}	Spacing between turns

ensure a stable output power with high efficiency. In mode B, the MI changes to $M_{\mathrm{P1S}}+M_{\mathrm{P2S}}$ as specified in Table II, whereas the voltage gain changes to $M_{\mathrm{Se}}G_{\mathrm{UUr}}$ accordingly. As shown in Fig. 4(b), a high MI or τ results in a high efficiency within certain ranges. By balancing the values of the MI and τ, the performance can become efficient in modes A and C. The efficiency is affected by M^* in mode B, especially when τ is low. $\eta^*\geq 1$ when M^* reaches a certain value from Fig. 4(b), which means that the transmission efficiency in mode B is not lower than that in other modes. To make the efficiency not decay in mode B, M^* should be higher than the critical value. The available values of M^* can be calculated by $\tau^*\geq 1$ ($k_{\mathrm{PSe}}{}^2 Q_{\mathrm{Lpe}}\geq k_{\mathrm{PSr}}{}^2 Q_{\mathrm{Lpr}}$). Thus, M^* should be equal to or higher than $\sqrt{2}$ in mode B to make $\tau^*\geq 1$, where $\tau^*\geq 1$ also represents that η of mode B is not lower than η of modes A and C.

III. EXTENDED TX COIL AND SEGMENTED OPERATION PARAMETER DESIGN

A. Design of Individual Tx Coil Segment for Stable Coupling

In the proposed system, each individual Tx coil is extended to provide an enlarged charging area for the compact Rx and to reduce the cost of hardware and control. To guarantee a stable charging performance, the MI between Tx and Rx coils should be stable in the enlarged charging area of each Tx coil segment. The layout of the proposed individual Tx coil segment and Rx coil is presented in Fig. 5, with its parameters and variables defined in Table III. The ferrites are attached to the Tx and Rx windings as in Fig. 5 to reduce leakage magnetic fields, which have the same sizes as the corresponding coils. To ensure an enlarged charging area in the moving direction and to avoid the adverse impacts on the system performance of any angular rotations, planar rectangular and circular coils are employed as the Tx and Rx coils, respectively [29]. The magnetic field produced by the Tx coil will be enhanced linearly with the ferrites [30]. The MI between the Tx and Rx coils is proportional to the interactive magnetic field. Accordingly, the ferrites do not affect the stable coupling area of MI. Thus, the MI performances of coupling coils without ferrites are mainly considered to simplify the coil design for stable coupling, and the same-size ferrites are added for restricting electromagnetic radiation once the winding parameters are determined.

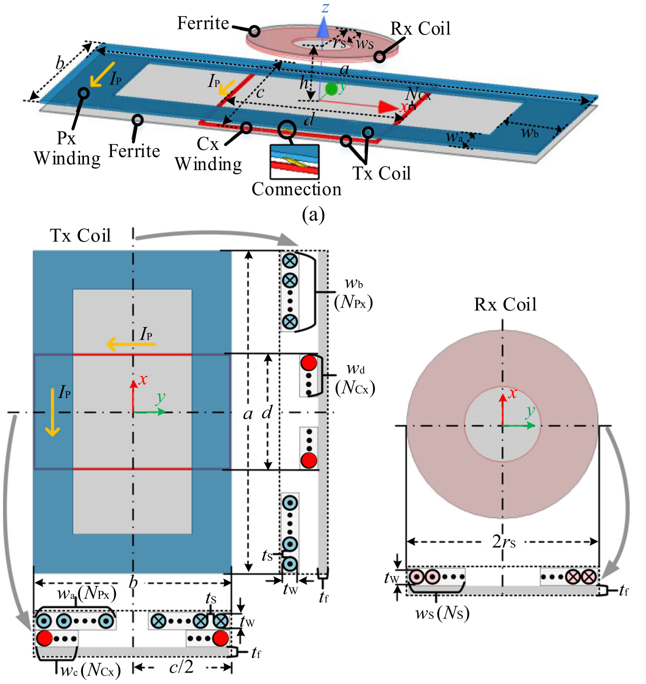

(a)

(b)

Fig. 5. Proposed coil structure. (a) Exploded view. (b) Top and cross-sectional views.

Each individual Tx coil segment is designed considering the moving charging area and lateral misalignment. The Tx coil segment mainly consists of a primary (Px) and a compensating (Cx) winding, as shown in Fig. 5. The Px and Cx windings are connected in series with the same current direction to regulate the equivalent MI between the Tx and Rx coils. The Px winding is designed to reduce the MI variations along the short side, whereas the Cx winding is designed to stabilize the MI along the long side. The movements along the long and short sides represent the moving and lateral misalignments, respectively. For the sake of design simplicity, the winding widths of the long and short sides are considered to be identical, i.e., $w_{\mathrm{a}} = w_{\mathrm{b}} = w_{\mathrm{Px}}$ and $w_{\mathrm{c}} = w_{\mathrm{d}} = w_{\mathrm{Cx}}$. The MI between any two coils without ferrites can be calculated by the summation of the MIs of individual parts of the coils [31]. Assume that a_{o} and b_{o} represent the outer length and the width of the Px winding, a_{i}

and b_i are the inner length and the width of the Px winding, and r_So and r_Si are the outer and the inner radii of the Rx coil, respectively. Based on the Neumann formula, the MI between the filaments of a_o side and r_so circle is calculated by

$$M_{\mathrm{PaS(o1,o1)}} = \frac{\mu}{4\pi}\oint_{l_\mathrm{P}}\oint_{l_\mathrm{S}}\frac{d\overrightarrow{l_\mathrm{P}}\cdot\overrightarrow{l_\mathrm{S}}}{|\overrightarrow{r_\mathrm{P}}-\overrightarrow{r_\mathrm{S}}|} = \frac{\mu}{4\pi}\int_{-\frac{a_\mathrm{o}}{2}}^{\frac{a_\mathrm{o}}{2}} \int_0^{2\pi}\frac{r_\mathrm{So}\cos\phi\, dx_1 d\phi}{\sqrt{\left(r_\mathrm{So}\cos\phi - x_1\right)^2 + \left(r_\mathrm{So}\sin\phi + \upsilon + \frac{a_\mathrm{o}}{2}\right)^2 + h^2}} \tag{13}$$

where υ is the horizontal displacement of the filaments. Similarly, the MIs between the filaments of other outer sides (b_o, a_o, b_o) and r_so circle can be obtained, where a_o and b_o represent the opposite sides of a_o and b_o. Subsequently, the MI between the outer filaments of the Px winding and the Rx coil can be calculated by

$$M_{\mathrm{PS(o1,o1)}} = \begin{pmatrix} M_{\mathrm{PaS(o1,o1)}} + M_{\mathrm{PbS(o1,o1)}} \\ +M_{\mathrm{P\hat{a}S(o1,o1)}} + M_{\mathrm{P\hat{b}S(o1,o1)}} \end{pmatrix}. \tag{14}$$

For any pair of nonmagnetic ferrite coils in Fig. 5, Lyle's equivalent method can be employed to calculate the MI [31], which replaces a coil with two equivalent filaments, with the MI being the product of MIs among the filaments and the number of turns. Based on Lyle's method, the MI is solely related to the number of turns once the outer and inner sides of coils are determined. The self-inductance calculation is similar to the MI determination [32]. Once the Rx coil parameters are specified, the expression for the MI can be simplified as

$$M_\mathrm{PS} = N_\mathrm{Px}N_\mathrm{S}\left(\frac{M_\mathrm{P(o1)S} + M_\mathrm{P(i1)S}}{2}\right) \tag{15}$$

where $M_\mathrm{P(o1)S}$ and $M_\mathrm{P(i1)S}$ represent the MIs between the equivalent outer and inner filaments of the Px winding and those of the Rx coil, respectively. Subsequently, the coupling coefficient of the coils can be expressed as

$$k_\mathrm{PS} = \frac{M_\mathrm{P(o1)S} + M_\mathrm{P(i1)S}}{\sqrt{\left(L_\mathrm{P(o1)} + L_\mathrm{P(i1)}\right)\left(L_\mathrm{S(o1)} + L_\mathrm{S(i1)}\right)}} \tag{16}$$

where $L_\mathrm{P(o1)}$, $L_\mathrm{P(i1)}$, $L_\mathrm{S(o1)}$, and $L_\mathrm{S(i1)}$ represent the self-inductances of the equivalent outer and inner filaments of the Px winding and the Rx coil, respectively. Based on (15) or (16), the MI or the coupling coefficient is stable if $M_\mathrm{P(o1)S}$+$M_\mathrm{P(i1)S}$ remains constant. Fig. 6 provides simulation results of the MI between a one-turn varied-size Px winding and a certain Rx coil with outer and inner filaments versus offsets in the *x* and *y* axes. Based on the MI profiles in Fig. 6, one can design the outer and inner filaments of the Px winding such that $M_\mathrm{P(o1)S}$+$M_\mathrm{P(i1)S}$ remains constant/stable. However, the MI profiles along the *x* and *y* axes are not identical because of the unequal long and short sides of the rectangular coil. Consequently, it is not trivial to find a group of outer and inner filaments to make $M_\mathrm{P(o1)S}$+$M_\mathrm{P(i1)S}$ along the *x* and *y* axes stable at the same time.

Based on the analysis of winding coupling characteristics, the Px winding is designed to make the MI along the short side (*y*-axis) stable, whereas the Cx winding is employed to compensate the MI peak in the center of the long side (*x*-axis). Based on the MI profile of different sides in Fig. 6, *c*:*d* = *a*:*b* is set to reduce the impact of the Cx winding on the MI along the short side. Meanwhile, to ensure an efficient transmission based on the analysis of Fig. 4 and a practical range for the quality factor, the coupling coefficient and MI between the Tx and Rx coils without ferrites should not be lower than 0.1 and 8 μH, respectively [33]. The operating frequency, airgap distance, Rx coil parameters, and width of Px winding are initially determined based on application requirements and constrictions. Winding width ratio $S = 2w_\mathrm{Px}/b$ is defined to simplify the design process of the Px winding, which is set to be within the range from 0.1 to 0.9 for implementation constrictions [34]. Subsequently, the Tx winding design flowchart can be summarized in the flowchart of Fig. 7 by the following three steps.

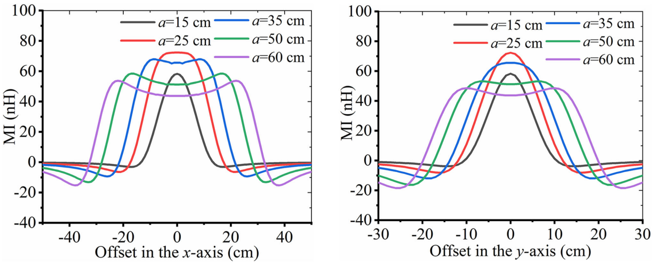

(a) (b)

Fig. 6. MI between a one-turn Px winding and a certain Rx coil with two filaments versus offsets when $r_\mathrm{so} = 7.5$ cm, $r_\mathrm{si} = 3$ cm, and *a*:*b* = 5:3 ($a_\mathrm{o} = a_\mathrm{i} = a$, $b_\mathrm{o} = b_\mathrm{i} = b$). (a) Offset in *x*-axis. (b) Offset in *y*-axis.

1) Prescreen the remaining dimension parameters (*a*, *w*Px) of the Px winding, which need to be calculated. By fixing the initial width *b* and sweeping *a* and *S* with the step sizes of Δa and ΔS, respectively, screen the possible dimension parameters. The parameter sweeping is to ensure that the coupling along the short side is stable and meets the minimum coupling coefficient condition. $k_{\mathrm{PS}(y\,=\,y\mathrm{max})} \geq k_{\mathrm{PS}(y\,=\,0)}$ and $y_\mathrm{max} \geq y_\mathrm{set}$ are to size the winding such that the stabilized coupling and required tolerance along the *y*-axis are met. y_max is the offset with maximum *k* in *y*-axis. y_set and k_set are the limits of misalignment tolerance and coupling coefficient, respectively. The coupling trend in *y*-axis is evaluated by (17), where γ is the limit of the coupling fluctuation. $k_{\mathrm{PS}(y\,=\,y\mathrm{max})} \geq k_\mathrm{set}$ and (17) are to guarantee the coupling efficient and stability

$$\frac{k_{\mathrm{PS}(y=y_\mathrm{max})} - k_{\mathrm{PS}(y=0)}}{k_{\mathrm{PS}(y=0)}} \leq \gamma. \tag{17}$$

The last two consecutive judgment/decision parts in the prescreening step in Fig. 7 are set as they can be corrected by different conditions.

2) Determine the parameters of the Px winding by evaluating the MI value and comparing the misalignment tolerance in the *x*-axis. Calculate the MI along the *x*-axis with $N_\mathrm{Px} = (w_\mathrm{P}+t_\mathrm{S})/(t_\mathrm{S}+t_\mathrm{W})$, where t_S is set to reduce the coil ESR. $M_{\mathrm{PS}(x\,=\,x\mathrm{max})} \geq M_{\mathrm{PS}(x\,=\,0)}$ and $M_{\mathrm{PS}(x\,=\,x\mathrm{max})} \geq M_\mathrm{set}$ are to enable a stable MI and an efficient power transmission.

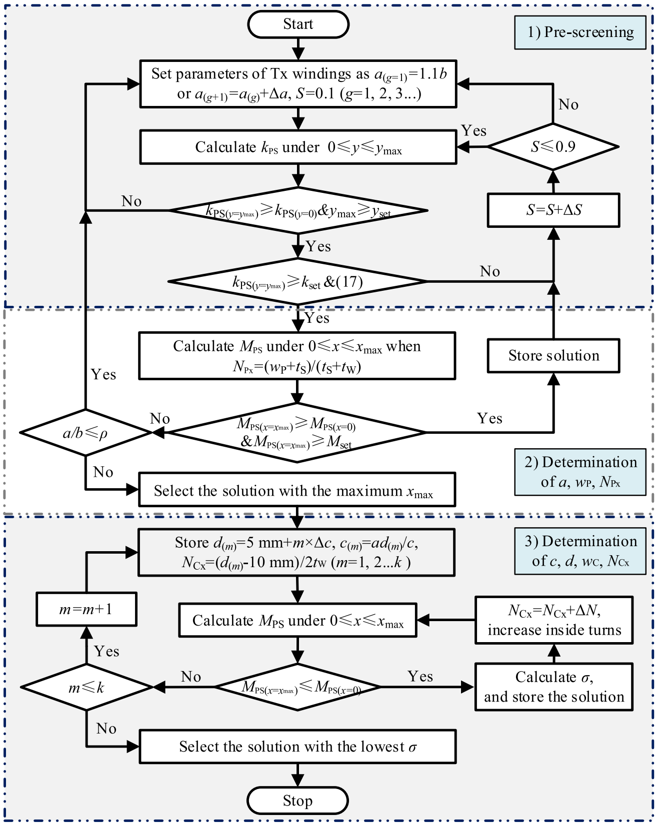

Fig. 7. Design flowchart of the extended Tx windings.

TABLE IV
PARAMETERS OF THE DESIGNED TX AND RX COILS

a	500 mm	N_{Cx}	1
b	300 mm	r_S	75 mm
c	300 mm	w_S	45 mm
d	180 mm	N_S	18
$w_a(=w_b)$	60 mm	t_W	2.5 mm
$w_c(=w_d)$	2.5 mm	t_S	1.92 mm
N_{Px}	14	h	50 mm

Subsequently, all possible solutions that meet this condition are stored until $a/b > \rho$. Ultimately, the solution with the maximum $x_{\max}$ is selected, which corresponds to a, w_P, N_{Px} of the Px winding with the maximum misalignment tolerance along the x-axis.

3) Determine the parameters of the Cx winding by evaluating the MI profile in the moving direction based on the calculation of standard derivation. According to the parameters of the Px winding, all possible parameters of the Cx winding are stored. The standard deviation σ of the MIs along the x-axis can be employed to evaluate the coupling stability [35]. Finally, the solution with the lowest σ, by which c, d, w_c, and N_{Cx} are determined, is selected.

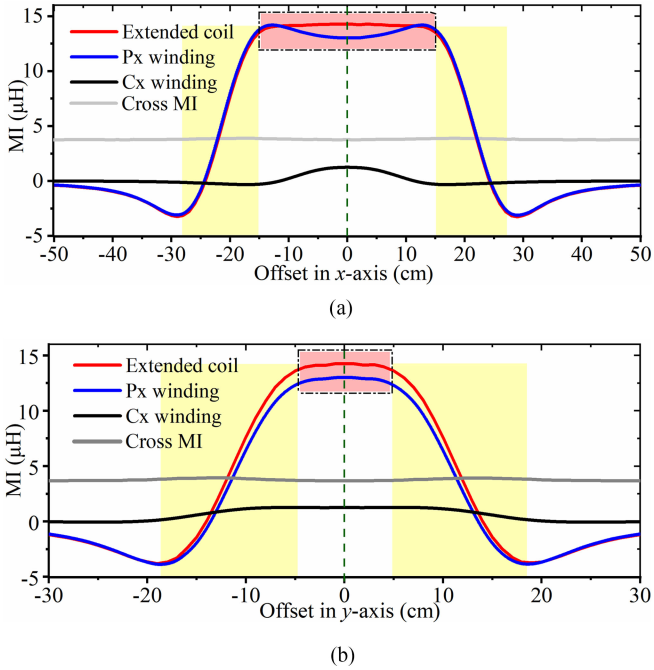

(a)

(b)

Fig. 8. MI between the designed Tx coil, Px and Cx winding and the Rx coil, MI between the windings versus offsets. (a) Offset in the x-axis. (b) Offset in the y-axis.

Based on the flowchart, the parameters of the Tx coil are obtained from a series of FEA-based simulations. Table IV provides the parameters of the designed windings. The thickness of ferrites t_f is determined as 1 mm according to the application and material limitations. The frequency is selected as 150 kHz to achieve an attainable quality factor [34]. Compared with the enlarged Tx coil designs in [23]–[26], the Tx coil segment with a simplified structure can be designed and implemented by simple and low-cost procedures. The coupling coefficient and MI, rather than the generated magnetic field, are directly employed for coupling stability evaluation. The efficient coupling coefficient and MI considerations are integrated into the design algorithm as it makes the design process simple and smooth.

Fig. 8 presents the MI between the extended Tx coil, Px and Cx winding, and the Rx coil with ferrites versus offset in the x or y axes. In Fig. 8, the red shadows represent the flat coupling (FC) regions, whereas the yellow shadows represent the MI falling/rising regions. As depicted in Fig. 8(a), the designed Tx coil produces an enlarged coupling area, whereas the Cx winding compensates the MI peak in the center of the Px winding in the x-axis. The Px winding makes the MI along the short side flat/stable, whereas the Cx winding only promotes the MI without any impact on its stability. The resultant performance in Fig. 8 is consistent with the analysis. The MI between the Px and Cx windings is also provided in Fig. 8. The self-coupling is unchanged under different offsets, and only the self-inductance of Tx coil increases with a fixed value.

The MI between the designed Tx and Rx coils versus offsets in the x and y axes is presented in Fig. 9. As shown, the MI is stable when the Rx locates in the FC area surrounded by the green lines. The design provides a ±15 cm charging range in the x-direction and a ±5 cm offset tolerance in the y-direction. The tolerance offset in the moving direction is four times the radius of the Rx coil, and the tolerance in the lateral misalignment meets the error requirement of autonomous moving equipment. The MI fluctuations in the FC area within ±2% from the results

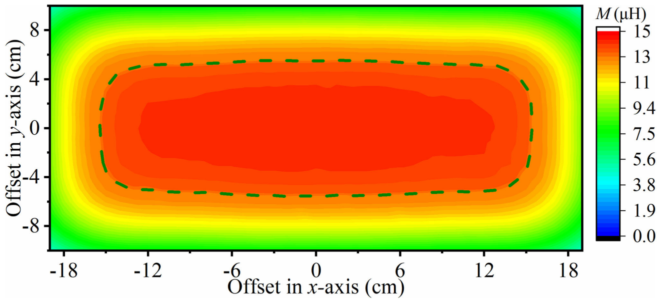

Fig. 9. MI between the designed Tx and Rx coils along the x and y axes.

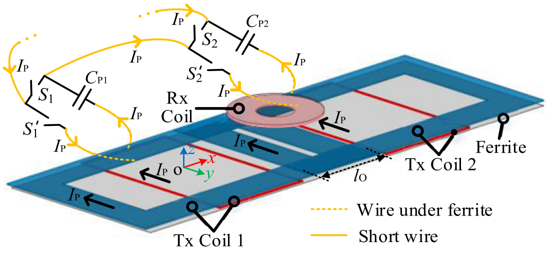

Fig. 10. Layout of the DWPT system with two Tx coil segments.

are shown in Figs. 8 and 9. If the required lateral misalignment tolerance, Rx coil size, or airgap distance changes according to the application conditions, based on the proposed method, the individual Tx coil segment can be redesigned flexibly for an extended charging range in the moving direction.

B. Design and Operation of the Segmented Tx Coils

Only one Tx coil is activated in modes A and C when the Rx locates in the FC region of either coil 1 or 2 in Fig. 1. Based on the designed single Tx coil segment, the transmission performance of the DWPT system with one Tx coil in operation is stable. In mode B, the Rx locates in the MI falling/rising region, in which the adjacent dual Tx coil segments are activated simultaneously to mitigate the fluctuation of transmission efficiency. Fig. 10 shows the model of the system with dual Tx coil segments, where l_{O} is the overlapping length. The synthetic MI from dual Tx coils and the cross MI between the adjacent Tx coils may affect the transmission performance. The wires for coil connection and turning OFF the useless coils are designed to be within the Tx coil area and be placed under the ferrite, and the wires outside the Tx coil area are designed to be as short as possible to reduce the magnetic field leakage in practical application, as shown in Fig. 10.

Fig. 11 provides the MIs of the DWPT system with dual Tx coils versus Rx position for various l_{O}, i.e, $l_{\mathrm{O}} = 0$, 5, 12.5, 14, and 20 cm. $l_{\mathrm{O}} = 12.5$ cm is the distance to decouple the dual Tx coil segments. $l_{\mathrm{O}} = 14$ cm is the critical value to make $M^{*} \geq \sqrt{2}$ in mode B based on the designed coil parameters, where τ in the MI falling/rising region with dual Tx coil segments becomes higher than that in the FC region with one Tx coil. The MIs between the dual Tx coil segments and the Rx coil and their sum are presented in Fig. 11(a) and (b), respectively. Based on the analysis in Section II, the sum of the MIs is the equivalent MI between the Tx and Rx when dual Tx coils operate, i.e., $M_{\mathrm{Se}} = M_{\mathrm{P1S}} + M_{\mathrm{P2S}}$. Based on Fig. 11(b), the FC region of a single Tx coil, due to the superposition of the MIs, is deteriorated if both Tx coil segments are activated simultaneously and remain active within the whole process. Thus, the dual Tx coil segments are activated simultaneously in the MI falling/rising regions (mode B). Additionally, the cross MI between the dual Tx coil segments is changed as the overlapping length changes. The cross MI would cause the changes of the equivalent inductance with one Tx coil or dual Tx coils. With the designed topology in Fig. 2, the varied impedances are tuned at ZPA input and load-independent output characteristics. Based on the analysis of the proposed topology, the compensation parameters of the Tx side are calculated and provided in Table V. X_3 is set as 12 Ω according to the voltage gain requirement. Two groups of solutions exist for the T type. Since ESRs of compensation capacitors are lower than those of the inductors, the capacitors are preferred as the components of choice over the inductors in the parameter determination process. Thus, the values in bold in Table V are selected as the final solution.

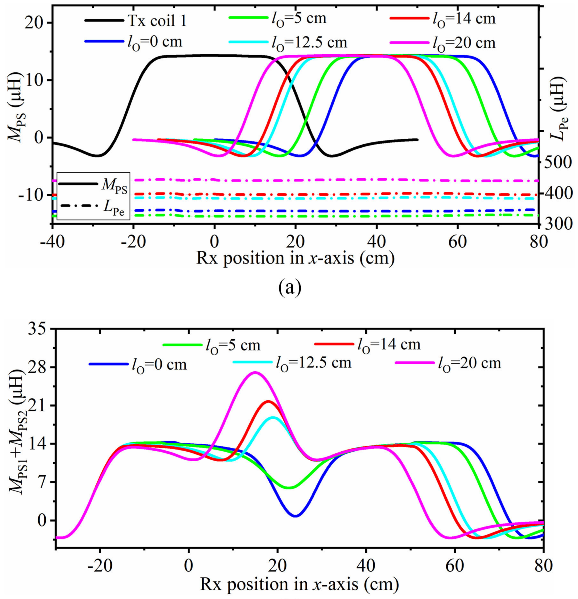

Fig. 11. MIs of the system with dual Tx coil segments versus Rx position in the x-axis under different overlapping lengths. (a) MIs from the dual Tx coil segments as well as their cross MI. (b) Sum of the MIs from the dual Tx coil segments.

TABLE V
PARAMETERS OF THE DESIGNED TOPOLOGY

l_O (cm)	M_{12} (μH)	C_P (nF)	$\|X_3\|$	X array	T type
0	-21.54	7.51	12	**[12, -28.60, -12]**; [-12, -52.60, 12.5]	**[*L*, *C*, *C*]**; [*C*, *C*, *L*]
5	-29.60	8.42	12	**[12, -43.79, -12]**; [-12, -67.79, 12]	**[*L*, *C*, *C*]**; [*C*, *C*, *L*]
12.5	≈0	5.83	12	[12, 12, -12]; **[-12, -12, 12]**	[*L*, *L*, *C*]; **[*C*, *C*, *L*]**
14	7.63	5.51	12	[17, 26.38, -17]; **[-17, 2.38, 17]**	[*L*, *L*, *C*]; **[*C*, *L*, *L*]**
20	28.43	4.51	12	[17, 65.59, -17]; **[-17, 41.59, 17]**	[*L*, *L*, *C*]; **[*C*, *L*, *L*]**

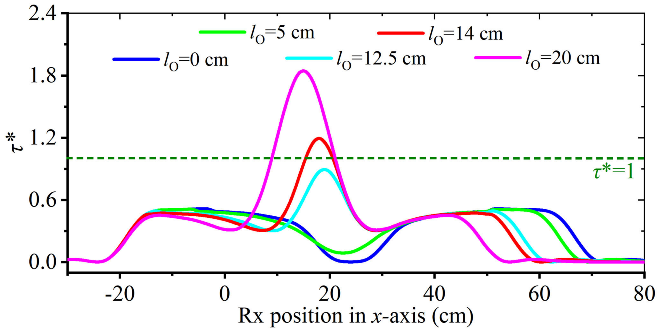

Fig. 12. τ^* of the DWPT system with dual activated Tx coil segments versus Rx position in the x-axis under different overlapping lengths.

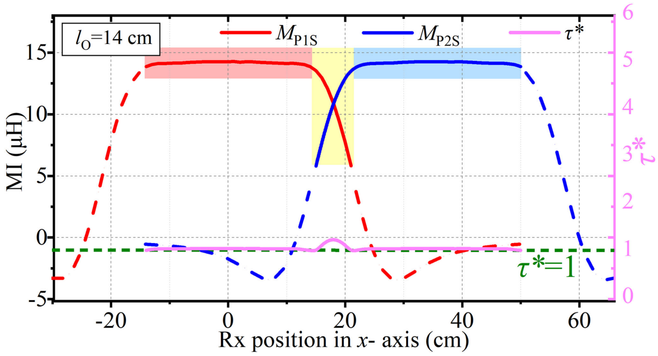

Fig. 13. MIs and τ^* of the DWPT system with dual Tx coil segments versus the Rx position in the x-axis when $l_{\mathrm{O}} = 14$ cm.

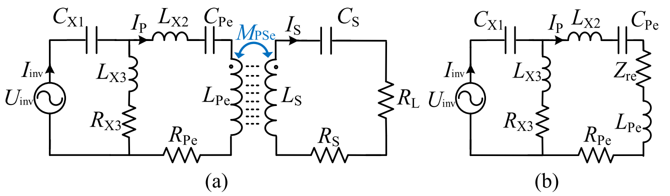

Fig. 14. Equivalent circuit models of the *CLL-S*/*S* compensated system. (a) Equivalent circuit model. (b) Rx reflected circuit model.

TABLE VI
PARAMETERS OF THE SYSTEM FOR SENSITIVITY ANALYSIS

Symbol	Values	Symbol	Values
C_{X1}	88.44 nF	L_{X2}	2.53 μH
L_{X3}	12.73 μH	R_{X3}	0.05 Ω
L_{Pe}	192.97 μH	R_{Pe}	0.39 Ω
C_{Pe}	5.41 nF	L_{S}	60.77 μH
R_{S}	0.10 Ω	C_{S}	18.53 nF

With the tuned topology, τ^* of the system with dual activated Tx coil segments versus the Rx position in the moving direction is presented in Fig. 12. It can be concluded that $l_{\mathrm{O}} = 14$ cm and 20 cm cause τ with dual Tx segments to be higher than that with one Tx segment. $l_{\mathrm{O}} \geq 14$ cm is the condition to make the efficiency not decay in mode B with dual Tx segments operating according to the superposition coupling characteristic. Yet, the total charging length is reduced with the increase of the overlapping length. Thus, $l_{\mathrm{O}} = 14$ cm, which is the critical value, is selected as the final overlapping length for an optimized charging length.

The MIs between the dual Tx coil versus the Rx position in the x-axis when $l_{\mathrm{O}} = 14$ cm are presented in Fig. 13 as well. In the red shadow region of Fig. 13, only coil 1 is activated. In the yellow shadow region, coils 1 and 2 are simultaneously activated. In the blue shadow region, only coil 2 is activated. τ^* of the DWPT system with the proposed operation strategy is also provided in Fig. 13. As it can be observed, the efficiency factor τ is relatively stable, and τ with dual activated Tx coil segments is not lower than that with one Tx coil.

C. Sensitivity Analysis of Transmission Performance to Compensation Tolerances

Based on the designed topology in Fig. 2 and the calculated parameters in Table V, the topologies under different operating modes are drawn as the same *CLL-S*/*S* compensated circuit model. Fig. 14(a) shows the equivalent circuit model considering the power loss of the inductances and coils, whereas Fig. 14(b) presents the Rx reflected circuit model. R_{X3} is the ESR of L_{X3}, and R_{Se} is the ESR of the Rx coil loop. R_{Pe} is the ESR of the Tx coil loop, and includes the coil ESR and switch contact resistance in this design. Z_{re} is the reflected impedance of the Rx, which can be obtained based on the loop current equations of I_{P} and I_{S}, expressed by

$$Z_{\mathrm{re}}=\frac{\omega^2{M_{\mathrm{PSe}}}^2}{jX_{\mathrm{S}}+R_{\mathrm{S}}+R_{\mathrm{L}}}=\frac{\pi^2\omega^2{M_{\mathrm{PSe}}}^2}{j\pi^2X_{\mathrm{S}}+\pi^2R_{\mathrm{S}}+8R_{\mathrm{load}}}. \tag{18}$$

Only the Tx coil loop parameters ($L_{\mathrm{Pe}}, R_{\mathrm{Pe}}, C_{\mathrm{Pe}}$) change when the segmented WPT system operates at different modes in Fig. 3. To facilitate the sensitivity analysis, the parameters of the system with one activated Tx coil are employed, which are obtained based on simulation as given in Table VI. The sensitivities of the impedance angle, output power, and efficiency under the compensation parameter tolerances are considered. Assume that the parameter tolerance is α, which means $C_{\mathrm{act}} = \alpha C_{\mathrm{res}}$. C_{act} is the actual value, and C_{res} is the calculated value from the condition of (4).

When the variation is capacitor C_{X1}, the input impedance can be obtained as

$$\begin{aligned}Z_{\mathrm{in\_}\alpha\mathrm{C_{X1}}}=&\frac{1}{j\omega\alpha C_{\mathrm{X1}}}\\&+\frac{(j\omega L_{\mathrm{X3}}+R_{\mathrm{X3}})\,(R_{\mathrm{Pe}}-j\omega L_{\mathrm{X3}}+Z_{\mathrm{re}})}{R_{\mathrm{X3}}+R_{\mathrm{Pe}}+Z_{\mathrm{re}}}.\end{aligned} \tag{19}$$

Then, the input impedance angle θ can be derived as

$$\theta_{\mathrm{in\_}\alpha\mathrm{CX1}}=\tan^{-1}\left[\frac{\mathrm{imag}(Z_{\mathrm{in\_}\alpha\mathrm{C_{X1}}})}{\mathrm{real}(Z_{\mathrm{in\_}\alpha\mathrm{C_{X1}}})}\right]. \tag{20}$$

Similarly, the input impedance angle expressions, when the variation is either C_{Pe}, C_{S}, L_{X2}, or L_{X3}, can be obtained. Based on the expressions, the impedance angle θ versus the parameter tolerances of C_{X1} C_{Pe}, C_{S}, L_{X2}, and L_{X3} can be calculated as shown in Fig. 15. Accordingly, the output power and transmission efficiency, when the variation is capacitor C_{X1}, are derived as (21a) and (21b), where [Z] is the impedance matrix expressed

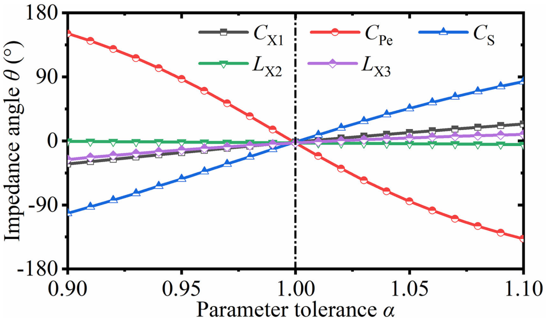

Fig. 15. Impedance angle θ versus the parameter tolerances of C_{X1}, C_{Pe}, C_S, L_{X2}, and L_{X3}.

as (21c)

$$P_{\mathrm{out\_}\alpha C_{X1}} = \left\{[Z]^{-1}(1,1)\cdot U_{\mathrm{inv}}\right\}^2 \cdot R_L \tag{21a}$$

$$\eta_{\alpha C_{X1}} = \left\{[Z]^{-1}(1,1)\right\}^2 \cdot |Z_{\mathrm{in\_}\alpha C_{X1}}| \cdot R_L \tag{21b}$$

$$Z = \begin{bmatrix} \frac{1}{j\omega\alpha C_{X1}} + j\omega L_{X3} + R_{X3} & -j\omega L_{X3} - R_{X3} & 0 \\ -j\omega L_{X3} - R_{X3} & R_{Pe} + R_{X3} & j\omega M \\ 0 & j\omega M & R_L + R_S \end{bmatrix}. \tag{21c}$$

$\{[Z]^{-1}(1,1)\}^2$ is defined as the normalized power to represent the trend of the output power according to (20a). Similarly, the output power and transmission efficiency expressions when the variation is either C_{Pe}, C_S, L_{X2}, or L_{X3} can be derived. Based on the expressions, the normalized power and efficiency versus parameter tolerances of C_{X1}, C_{Pe}, C_S, L_{X2}, and L_{X3} can be obtained as shown in Fig. 16.

From the results in Figs. 15 and 16, the parameter tolerances of C_{X1}, L_{X2}, and L_{X3} have less impacts on the transmission performances, and the parameter sensitivities are low. Yet, the sensitivities of C_{Pe} and C_S, which are included in the coil loops are relatively high. The tolerances of C_{Pe} and C_S substantially degrade the transmission performance including ZPA performance, output power, and efficiency. The characteristic of the compensation capacitors in the coil loops is like the similar components in the *LCC-S* compensated topology [35], [36]. To avoid the influence of the sensitive capacitors, antivariation connection or high-performance capacitor can be employed, and the capacitor tolerance can be less than ±0.5% [37]. The analysis provides a reference of the compensation component selections, and the sensitive components in the designed topology are similar to other common compensations.

IV. SYSTEM CONTROL WITH POSITION DETECTION AND POWER REGULATION

A. *Position Detection and Power Stabilization Method*

In the proposed operating strategy, detection of the position of the Rx is necessary to switch the Tx coil segments ON or OFF. With the strategy and parameters described in the previous section, the transmission efficiency would be stable or improved as the Rx moves. However, compared with the output power in the FC region of one activated Tx coil, the synthetic MI of the dual Tx coils as shown in Fig. 11 is changed. Consequently, the control method with the Rx position detection and power regulation capability is studied to configure/coordinate the segmented Tx coils and stabilize the output power. According to the Rx reflected circuit model in Fig. 14(b), U_{inv} and I_{inv} are deduced by

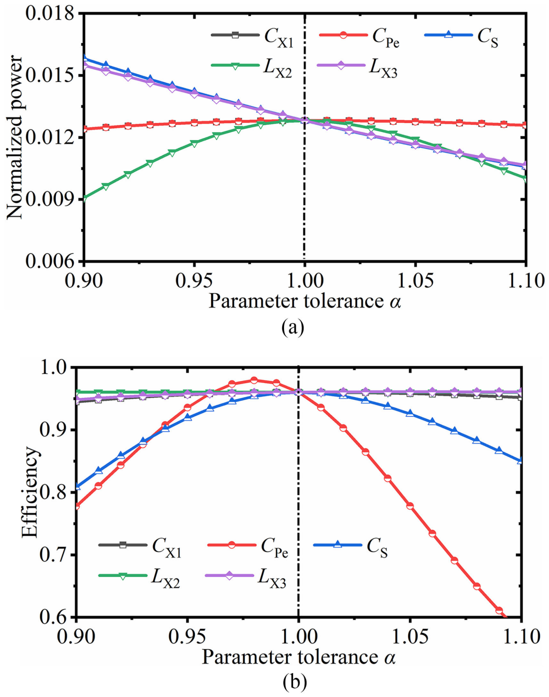

(a)

(b)

Fig. 16. Normalized output power and efficiency versus the parameter tolerances of C_{X1}, C_{Pe}, C_S, L_{X2}, and L_{X3}. (a) Normalized output power. (b) Efficiency.

$$U_{\mathrm{inv}} = \frac{I_P\left(\omega^2 {L_{X3}}^2 - 2j\omega L_{X3}R_{X3} + R_{X3}R_{Pe} + R_{X3}Z_{re}\right)}{j\omega L_{X3} + R_{X3}} \tag{22a}$$

$$I_{\mathrm{inv}} = \frac{j\omega I_P L_{X3} + I_P R_{X3} + U_{\mathrm{inv}}}{R_{X3}}. \tag{22b}$$

Based on the relation of the input and output of the phase-shifting modulation based inverter, U_{inv} can be obtained with the DC input voltage U_{IN} and the phase-shifting angle α. I_{inv} also can be calculated with the dc input current I_{IN} due to the basic equal input and output power of the inverter. Thus, the root-mean-square values of the fundamental components of U_{inv} and I_{inv} can be calculated by

$$|U_{\mathrm{inv}}| = \frac{2\sqrt{2}U_{\mathrm{IN}}\sin\left((\pi-\alpha)/2\right)}{\pi} \tag{23a}$$

$$|I_{\mathrm{inv}}| \approx 1.1 I_{\mathrm{IN}} \tag{23b}$$

where U_{IN} is the voltage of the constant dc source, and α is modulated by the controller. The values of U_{IN} and α can be considered as known in the controller. To calculate $|I_{\mathrm{inv}}|$, the only variable that needs to be identified is I_{IN}, which can be sensed easily. Besides, the equivalent circuit parameters of

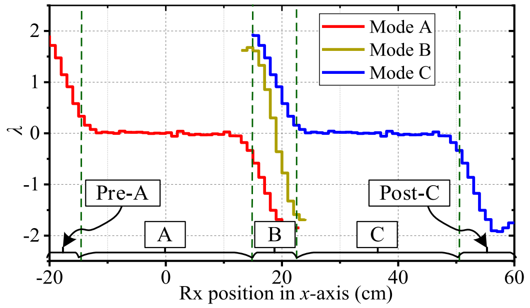

Fig. 17. λ_{P} versus Rx position in the x-axis with the designed operating strategy.

compensation components and the ESR of the Tx coil loop in (22) are regarded as constants in normal operation, which can be recorded in the controller [38]–[40]. Based on (22) and (23), Z_{re} is deduced as

$$Z_{\mathrm{re}}=\frac{\begin{array}{c}\pm\sqrt{-4\omega^2q^4{L_{\mathrm{X3}}}^2{R_{\mathrm{X3}}}^4+p^2q^2\left(\omega^2{L_{\mathrm{X3}}}^2+{R_{\mathrm{X3}}}^2\right)^2}\\+\left(p^2-\omega^2q^2{L_{\mathrm{X3}}}^2\right)R_{\mathrm{X3}}-q^2{R_{\mathrm{X3}}}^2R_{\mathrm{Pe}}+p^2R_{\mathrm{Pe}}\end{array}}{-p^2+q^2{R_{\mathrm{X3}}}^2} \tag{24}$$

where $p=|U_{\mathrm{inv}}|$, $q=|I_{\mathrm{inv}}|$. Z_{re} can be calculated with the recorded or measurement parameters. Between the two solutions in (24), the one with the minus sign is selected over the other one, which is almost zero based on the ranges of the variables. Subsequently, based on (18), M_{PSe} can be calculated by

$$M_{\mathrm{PSe}}=\frac{\sqrt{Z_{\mathrm{re}}(\pi^2R_{\mathrm{Se}}+8R_{\mathrm{load}})}}{\pi\omega}. \tag{25}$$

The equivalent load of battery R_{load} does not vary significantly within a short period. R_{load} can be calculated based on the information of U_{out} and I_{out} from the battery management system of the autonomous moving equipment [5]. The required real-time information of the Rx for calculation of R_{load} at the Tx side is not high. Similar to the ESR of the Tx coil loop, the ESR R_{Se} of the Rx coil loop can also be initially defined in the controller. Then, the MI between the Tx and Rx coils can be estimated at the Tx controller side from (24) and (25) based on the known information and measured dc input current. However, the estimated MI at one point cannot represent the accurate position in the DWPT system because of the symmetrical profile in Fig. 17. As modes A, B, and C are dynamically switched during the dynamic charging process, not only the current Rx position but also the upcoming region should be detected for the segmented Tx configuration. Nevertheless, the position detection should be performed online during moving and charging. Switching the Tx coils to detect the position of Rx is not practical as it would affect the charging performance.

According to the MI variation trends in Fig. 13, a dynamic position factor λ_{P}, which represents the slope of MI variation trend, is defined as (26a) to detect the Rx position in real time. Then, the dynamic position factor can be calculated by (26b) based on (25). In (26), x is the position along the x-direction of the Tx coil, and subscripts "P" and "P–1" represent the current and the previous detection points, respectively. x_{P} is the distance between the points P and (P–1), which can be acquired directly as it is essential information for the automation equipment [4], [5]

$$\lambda_{\mathrm{P}}=\frac{M_{\mathrm{PSe(P)}}-M_{\mathrm{PSe(P-1)}}}{x_{\mathrm{P}}-x_{\mathrm{P-1}}} \tag{26a}$$

$$\lambda_{\mathrm{P}}=\frac{\sqrt{(\pi^2R_{\mathrm{Se}}+8R_{\mathrm{load}})}\left(\sqrt{Z_{\mathrm{re(P)}}}-\sqrt{Z_{\mathrm{re(P-1)}}}\right)}{\pi\omega\Delta x_{\mathrm{P}}}. \tag{26b}$$

For the operation strategy of Fig. 13, λ_{P} versus the Rx position in the x-axis can be obtained as Fig. 17. As shown in Fig. 17, the Rx position with current location and upcoming regions can be detected by the estimated λ.

Based on the voltage gain of (5), the values of $|U_{\mathrm{S}}|$ and P_{out} can be calculated by

$$|U_{\mathrm{S}}|=\frac{2\sqrt{2}\omega U_{\mathrm{IN}}M_{\mathrm{PSe}}\sin\left((\pi-\alpha)/2\right)}{\pi X_3} \tag{27a}$$

$$P_{\mathrm{out}}=\frac{\omega^2{M_{\mathrm{PSe}}}^2{U_{\mathrm{IN}}}^2\sin^2\left((\pi-\alpha)/2\right)}{{X_3}^2R_{\mathrm{load}}} \tag{27b}$$

where M_{PSe} may change under different operating modes. With the designed Tx coils, M_{PSe} can be regarded as constant in modes A and C. Yet, it becomes $M_{\mathrm{P1S}}+M_{\mathrm{P2S}}$ in mode B with the dual activated Tx coil. The phase-shifting angle of the system can be modulated to stabilize the output power as (28a), where e is calculated by (28b). In (28), the subscripts "mode_A" and "mode_B" refer to the corresponding parameters in modes A and B, respectively. N is the number of the estimated MI points in mode A

$$\alpha_{\mathrm{mode\_B}}=\pi-2\arcsin\left(e\cdot\sin\left((\pi-\alpha_{\mathrm{mode\_A}})/2\right)\right) \tag{28a}$$

$$e=\frac{\sum_{i=1}^{N}M_{\mathrm{PS\_mode\_A}(i)}}{N\cdot M_{\mathrm{PS\_mode\_B}}}. \tag{28b}$$

B. System Control Scheme

Based on the position detection and power regulation method, the system control flowchart is illustrated in Fig. 18. The information regarding the coordination of the autonomous moving equipment is delivered to the management center (MC) for status monitoring. The MC commands the DWPT system when the equipment to be charged is close to the Tx [5]. The variable *ENT*, which represents whether the Rx is near the Tx, is set as 1 in the controller when the Rx is approaching. Then, the remaining of the flowchart in Fig. 18 begins. In the flowchart of Fig. 18, λ_{lim} is the set limit to determine the position of Rx based on the profiles in Fig. 17. A constant threshold value of the MI, i.e., M_{PSlim}, is employed to avoid any impact on the determination of λ when the Rx locates in any extreme edge of the Tx coil, e.g., $x>\pm30$ cm in Fig. 8(a). α_{req} is the phase-shitting angle in mode A or C according to the power requirement. The flowchart of Fig. 18 is divided into the following steps.

1) Initialize *Mode* = A, $n=1$, and $\alpha=\alpha_{\min}$ when Rx initially enters the charging area. α is set as $\alpha_{\min}$ to reduce the power loss when Rx does not locate in the efficient region. If $n>1$, meaning that the procedure is not in the initial cycle, preserve $\alpha=\alpha_{\mathrm{req}}$ to avoid power fluctuation in the

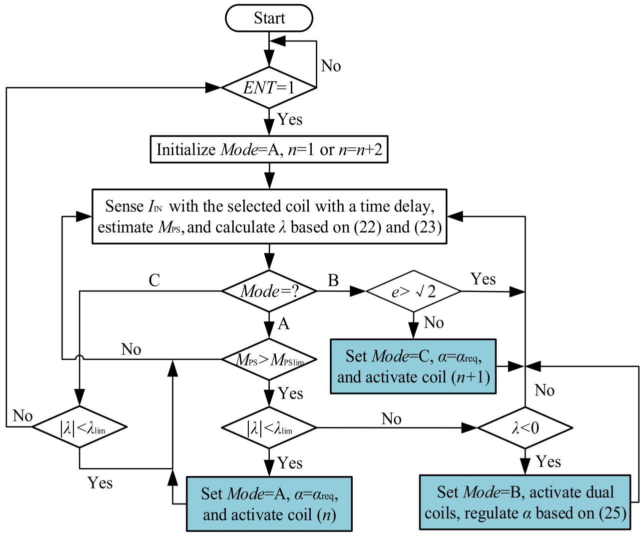

Fig. 18. Flowchart of the system control with position detection and power regulation.

TABLE VII
VOLTAGE AND CURRENT RATING RATIOS WHEN TX COIL 1 IS ACTIVATED AND TX COILS 1 AND 2 ARE ACTIVATED

Switch	Coil 1 is activated			Coils 1 and 2 are activated		
	Status	Voltage (Coil/Inverter)	Current (Coil/Inverter)	Status	Voltage (Coil/Inverter)	Current (Coil/Inverter)
S_1	OFF	3.832/1	1.342/1	OFF	3.023/1	1.444/1
S_1'	ON	3.832/1	1.342/1	ON	3.023/1	1.444/1
S_2	ON	3.832/1	1.342/1	OFF	3.023/1	1.444/1
S_2'	OFF	3.832/1	1.342/1	ON	3.023/1	1.444/1
				…		
S_n	ON	3.832/1	1.342/1	ON	3.023/1	1.444/1
S_n'	OFF	3.832/1	1.342/1	OFF	3.023/1	1.444/1

dynamic charging process. Then, sense I_{IN} when the first Tx coil is activated, estimate M_{PS} and calculate λ based on (25) and (26).

2) Determine the operation mode, and activate any of the corresponding Tx coil segments. If *Mode* = A, compare M_{PS} and M_{PSlim}. When $M_{\mathrm{PS}}<M_{\mathrm{PSlim}}$, jump to Step 1 and continue to estimate M_{PS} with the moving Rx until $M_{\mathrm{PS}}\geq M_{\mathrm{PSlim}}$. Then, compare |λ| and λ_{lim}. If $|\lambda|<\lambda_{\mathrm{lim}}$, set *Mode* = A, $\alpha = \alpha_{\mathrm{req}}$ and activate coil 1 or *n*. If $|\lambda|\geq\lambda_{\mathrm{lim}}$ and λ<0, set *Mode* = B, regulate α based on (26) and activate Tx coils as the strategy of mode B. Otherwise, jump to Step 1 as the flowchart. If *Mode* = B, compare the value of *e* and $\sqrt{2}$. $e\geq\sqrt{2}$ means the Rx locates in the efficient region of mode B in Fig. 14. Otherwise, the position is in the FC region of mode C. Then, set *Mode* = C, $\alpha = \alpha_{\mathrm{req}}$, and activate coil 2 or (*n*+1).
3) When *Mode* = C, maintain the state if |λ|<λlim. Otherwise, enter the next cycle as the flowchart and set $n = n+2$. *ENT* is cleared when either the equipment leaves the dynamic charging area or the value of *n* exceeds the number of Tx coils.

Owing to the segment strategy with at least one Tx coil activated in the whole charging process, the transient output power will not be zero. Due to the relatively long action time of the relay, the output power fluctuates at the moment of switching. To prevent the adverse impact of high-power pulse in the switching, the phase-shifting angle is modulated to be in the two-coil mode once the switching signal from one Tx coil operation mode to two Tx coil operation mode is generated. In addition, the phase-shifting angle is modulated to be in the one-coil mode with a relay switching delay when the switching signal from two Tx coil operation mode to one Tx coil mode is generated.

The proposed system control determines the Rx position and regulates the output power in the transition region by monitoring a single dc input current. With the control, the segmented Tx coils are configured/coordinated and the output power pulsation is mitigated at the Tx side effectively.

C. Voltage and Current Evaluation of Coil Switches

The voltage and current on the segmented Tx coil switches (S_{n} and S_{n}') are evaluated to explain the feasibility of the topology design in Fig. 2. The voltage and current of the DWPT system with *n* segmented Tx coils when one Tx coil is activated or dual Tx coils are activated are analyzed. Based on the loop current and voltage deductions, the peak-to-peak voltage and current ratios between the coil switches in the proposed DWPT system with *n* Tx coils and the inverter switches in the system with *n* full-bridge inverters driving *n* Tx coils can be obtained. The maximum peak-to-peak voltage and current of the switches can be selected as the rating values. Based on the equivalent parameters of the designed system in Table VI, the voltage and current ratings of the coil switches versus the switches of the *n* full-bridge inverters can be obtained. Table VII presents the coil switch status, the voltage and current rating ratios between the coil switches and the full-bridge inverter switches when the Tx coil 1 is activated, and when the Tx coils 1 and 2 are activated. The peak-to-peak voltage and current on the inverter switch are half of the output voltage and current of the full-bridge inverter. The maximum voltage and current ratings are selected as the references for device selection. Thus, the voltage and current ratings of the coil switches are about 1.92 and 0.72 times of the maximum peak-to-peak values of the inverter output voltage and current, respectively. The capacitor C_{Pn}, which is connected to each coil segment in series in the proposed topology, reduces the voltage stress on the nonconducting switches. Consequently, the voltage and current ratings stay within an acceptable range and commonly used switches can meet the current/voltage requirements of the proposed topology.

V. EXPERIMENTAL VERIFICATION AND SYSTEM COMPARISON

A. Prototype Setup

To verify the performance and effectiveness of the proposed system, a DWPT prototype with two Tx coil segments is implemented as presented in Fig. 19, with the detailed parameters

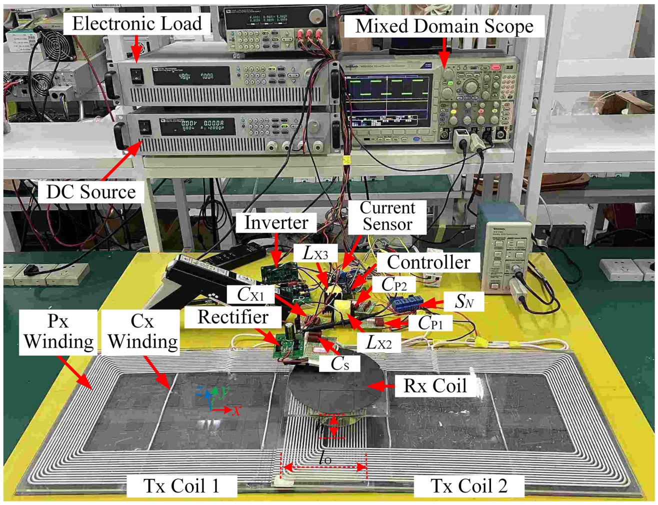

Fig. 19. Implemented experimental prototype.

TABLE VIII
PARAMETERS OF THE EXPERIMENTAL PROTOTYPE

Symbol	Values	Symbol	Values
U_{IN}	48 V	R_{P2}	0.19 Ω
C_{X1}	88.35 nF	C_{P2}	5.26 nF
L_{X2}	2.99 μH	M_{12}	8.25 μH
R_{X2}	0.02 Ω	L_S	55.10 μH
L_{X3}	13.51 μH	R_S	0.12 Ω
R_{X3}	0.10 Ω	C_S	20.69 nF
L_{P1}	194.40 μH	R_{load}	12 Ω
R_{P1}	0.27 Ω	h	5 cm
C_{P1}	5.36 nF	f	150 kHz
L_{P2}	198.50 μH	l_O	14 cm

provided in Table VIII. In the proposed segmented strategy, the two Tx coils with operating modes A, B, and C can be regarded as a typical unit in the dynamic charging process. In the DWPT system with more Tx coil segments, it there are multiple typical units. The circuit of the experimental prototype is the same as the one in Fig. 2 with a *T*-series/series topology. A phase-shifting modulation based full-bridge inverter serves as the dc to ac converter. Omron relays are employed in the prototype. The ESR and voltage drop of the relay are lower than another common switch scheme, which consists of two inverse series-connected MOSFETS [27]. The two Tx coil segments 1 and 2 and one Rx coil are fabricated with their parameters listed in Table IV. TDK PC 95 ferrites with 1 mm thickness and same plane dimensions are attached to the coils for restricting electromagnetic radiation. The system control with its position detection and power regulation in Section IV is coded/implemented on an STM32 controller. A pair of Bluetooth communication modules of HC-08 are adopted to transfer the information from Rx to Tx for MI estimation. Hall-effect current sensors are employed to measure the dc input current. The gap distance of the Tx and Rx is 5 cm, which is suitable for automatic moving robots in substations.

Due to the switching relay that is connected in series with the coil loop and the connection wires, as shown in Fig. 2, the ESR of the Tx coil loop is increased. The additional resistance can be considered as a part of the coil loop ESR, and the ESR of one Tx coil is nearly four times of the relay contact and connection wire resistances. In the parallel DWPT schemes with switchable inverters in [10]–[16] and [18], the number of Tx coil loops linked to one inverter is limited to reduce the high-frequency power loss on connection wires. Similar to the parallel scheme, the number of Tx coil loops in this segmented system is limited to minimize the impact on transmission efficiency. The efficiency decreases within 2.5% when the number of segmented Tx coils is less than 5 compared to the system with a single Tx coil. The limited number of Tx coil loops fed by one inverter cause little impact on the efficiency. The charging length can be further extended by increasing the inverter and topology. Besides, the current through the switches with the operating frequency would not cause any abnormal heating when they operate normally.

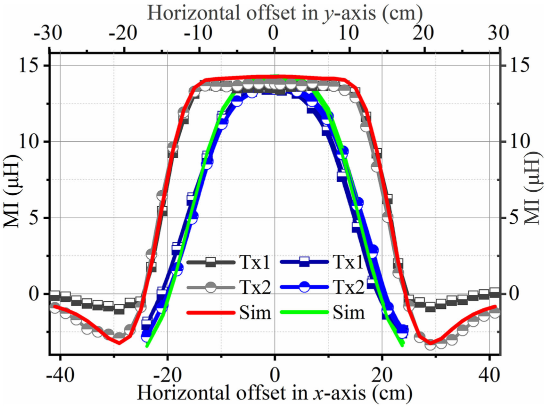

Fig. 20. Experimental and simulated MIs between the two single Tx coils and the Rx coil versus offset in the *x* and *y* axes.

B. Experimental Results

Fig. 20 provides the measured and simulated MIs between the two single Tx coil segments and the Rx coil versus the offsets in the *x* and *y* axes. As can be observed, the fabricated Tx coils with the designed parameters produce a stable MI when the offset ranges from –15 to 15 cm along the *x*-axis and from –5 to 5 cm along the *y*-axis. The experimental results are closely matched with those from simulations. The effective dynamic charging length produced by an individual Tx coil segment is four times the radius of the Rx coil.

The efficiency of the WPT system, i.e., the stage before the inverter to that after the rectifier, with Tx coil 1 or 2 versus offset in *x* and *y* axes is tested with the results presented in Fig. 21. It can be concluded that the efficiency within the FC region is stable, and its profile is similar to the MI results in Fig. 20. The efficiency in the FC region reaches 87.6%, whereas the corresponding efficiency of the stage after the inverter to that before the rectifier is higher than 90%. This is higher than the asymmetric coil designs reported in [23] and [24]. The simplified Tx coil design in this article provides an enlarged dynamic charging area with stable and efficient performance.

Fig. 22 presents U_{inv} and I_{inv} waveforms of the DWPT system with the conventional and the proposed topologies under different operation modes when $\alpha = 60°$. In the conventional

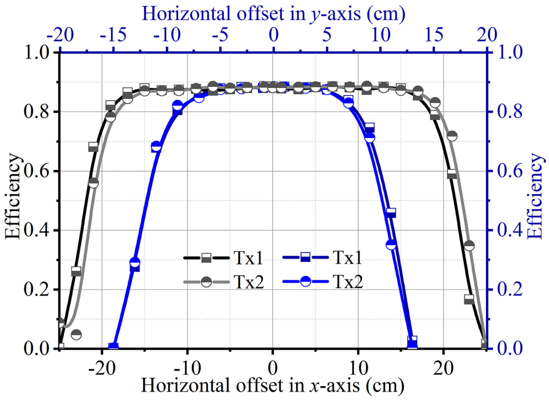

Fig. 21. Efficiency of the WPT system with each Tx coil versus offset in the *x* and *y* axes.

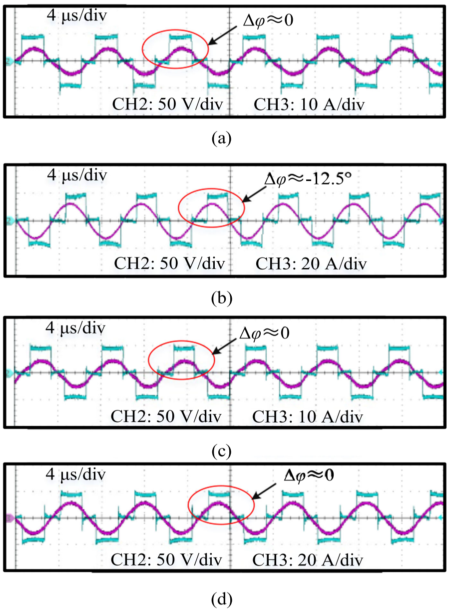

(a)

(b)

(c)

(d)

Fig. 22. U_{inv} and I_{inv} waveforms of the system based on the conventional and the proposed topologies under different operation modes. (a) Conventional topology with one Tx coil in operation. (b) Conventional topology with dual Tx coils in operation. (c) Proposed topology with one Tx coil in operation. (d) Proposed topology with dual Tx coils in operation.

topology without considering the cross MI of the dual activated Tx coils, the capacitor of each Tx coil loop is set to tune the single coil. If the coils are decoupled, the conventional topology would be tuned with the dual Tx coils. However, the presence of the cross MI would cause detuning. As shown in Fig. 22(a) and (b), the conventional topology with one Tx coil is tuned, whereas the one with dual Tx coils is not. Owing to the proposed *T*-series/series topology, as shown in the waveforms in Fig. 22(c) and (d), the DWPT system is tuned with an approximate ZPA input under different modes with either one Tx activated coil or two activated ones.

The measured and estimated λ of the designed DWPT system when the Rx moves along the *x*-axis are presented in Fig. 23. The values in the operation region of the designed strategy are closely matched. The differences in the edge region, which is not in the designed charging area, have no impact on the system

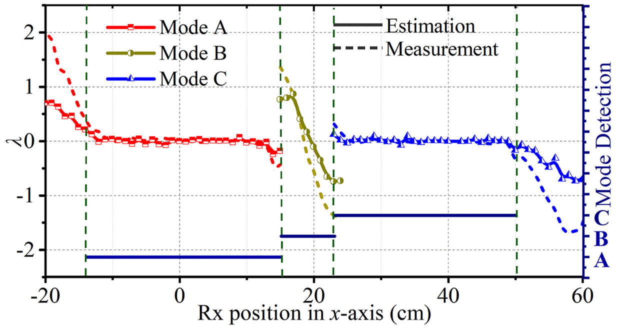

Fig. 23. Measured or estimated λ of the DWPT system, and the detected mode in the controller.

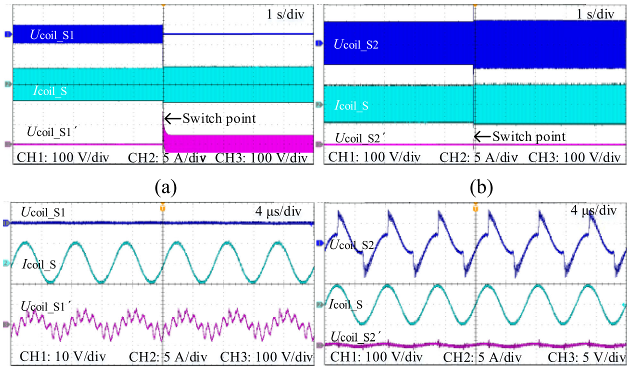

(a) (b)

(c) (d)

Fig. 24. Voltage and current waveforms of the switches S_1, S_1', S_2, and S_2'. (a) Switching of S_1 in S_1' from mode B to mode C. (b) Switching of S_2 in S_2' from mode B to mode C. (c) S_1 in S_1' in mode C. (d) S_2 in S_2' in mode C.

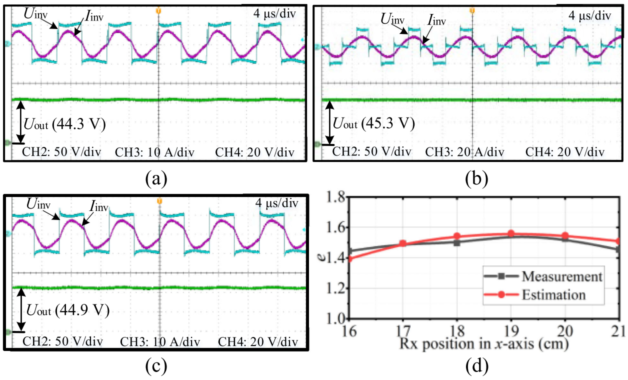

(a) (b)

(c) (d)

Fig. 25. U_{inv}, I_{inv}, and U_{out} waveforms of the system with the proposed control under different operating modes, and the value of *e* versus the Rx position. (a) Mode A with Tx coil 1. (b) Mode B with the dual Tx coils. (c) Mode C with Tx coil 2. (d) Calculated *e* versus the Rx position in mode B based on measurement and estimation.

control. Based on the estimated values, the detected mode in the controller shown in Fig. 23 is consistent with the proposed strategy in Fig. 13, thereby confirming the effectiveness of the proposed position detection method.

Experimental voltage and current waveforms of the switches S_1, S_1', S_2, and S_2' in different operating stages are captured. Fig. 24 provides waveforms of the switches S_1, S_1', S_2, and S_2' in modes B and C to briefly describe the voltage stress on

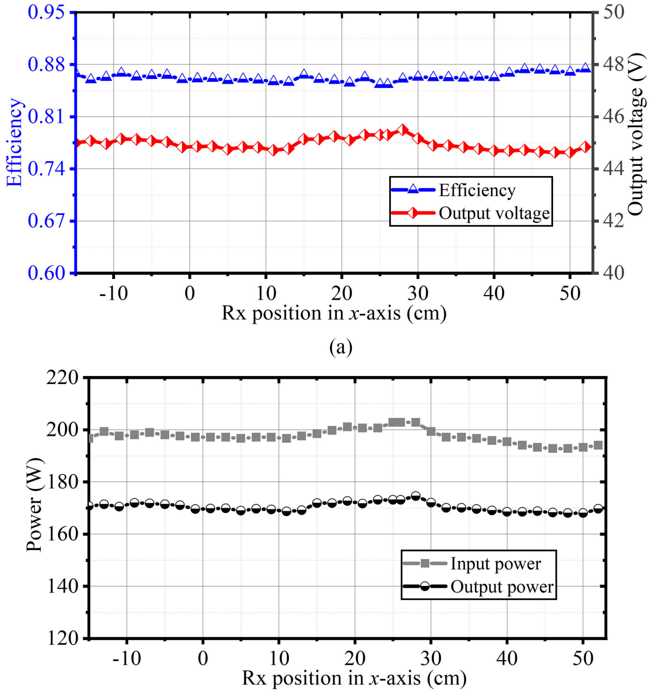

(a)

(b)

Fig. 26. Performance of the designed DWPT system with the proposed control when the Rx moves along the *x*-axis. (a) Efficiency and output voltage. (b) Input and output powers.

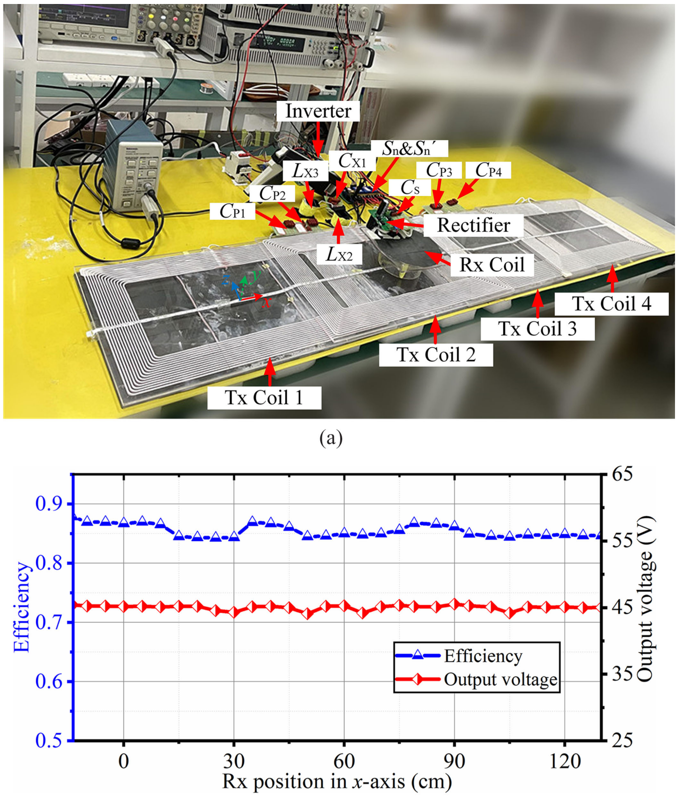

(a)

(b)

Fig. 27. Experimental DWPT prototype with four segmented Tx coils and the measured efficiency and output voltage when the Rx moves along the *x*-axis. (a) Experimental prototype. (b) Efficiency and output voltage.

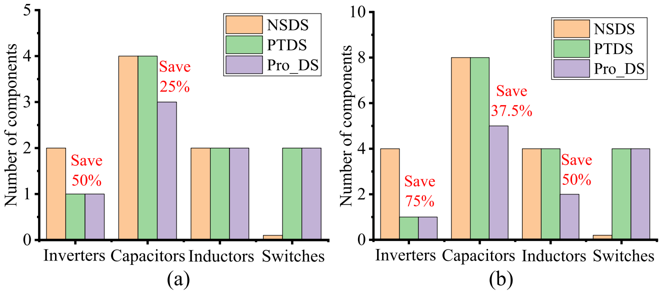

(a)

(b)

Fig. 28. Number of components used in three DWPT systems with a high-order compensation topology when two or four Tx coil segments are employed. (a) Two Tx coil segments. (b) Four Tx coil segments.

the switches. Fig. 24(a) and (b) shows the switching waveforms when the Rx just quits the transition region from mode B to mode C. Fig. 24(c) and (d) presents the waveforms of the switches in mode C when the Rx locates in the stable coupling area of the Tx coil 2. The voltage on the nonconducting switches of the inactivated Tx coils in Fig. 24(d) is induced by the cross MI from the activated Tx coil, and the irregular waveforms are caused by the oscillation of the inactivated coils and capacitors in series. From the results, the relay switches operate normally, and the maximum peak-to-peak voltage of the coil switches is about two times of the inverter output voltage. The voltage stress on the coil switches is commonly acceptable, which is similar to the analysis results and is consistent with the design objectives.

U_{inv}, I_{inv}, and U_{out} waveforms of the DWPT system with the control under operating modes A, B, and C are presented in Fig. 25(a)–(c). The waveforms are acquired when the Rx locates in (0 cm, 0 cm) under mode A with Tx coil 1 operation, (19 cm, 0 cm) under mode B with dual activated Tx coils, and (46 cm, 0 cm) under mode C with Tx coil 2 operating. It can be concluded that the output voltages are almost constant. Fig. 25(d) provides the calculated e in mode B versus the Rx position based on measurement and estimation. The estimated value determines the accuracy of power regulation in mode B from (28). The estimated and the actual measured values are consistent with the results in Fig. 25(d), and the tolerances at the edges are lower than 3.6%. The control with voltage regulation is verified by the results.

Fig. 26 shows the efficiency, output voltage, and input and output powers of the DWPT system with the control when the Rx moves from –15 to 53 cm along the *x*-axis. The experimental efficiency is around 87% when the output power is about 167 W, i.e., the power to energize autonomous moving equipment such as an inspection robot. The output power would feed the equipment effectively as the motion of these types of equipment is relatively slow in the meticulous inspection working area. The results in Fig. 25 show that both the efficiency and the output voltage of the designed DWPT system are reasonably stable during the movement, with fluctuations limited within $\pm 2\%$. The charging area length produced by the DWPT system with two Tx coil segments is about nine times the radius of the Rx coil.

To verify the performance of the proposed system with more segmented Tx coils, two extra Tx coils with the designed

TABLE IX
Comparison With the Previous Work in [9], [10], [12]–[20] ("-" Means Not Given)

Ref.	Scheme (Compensation)	ZPA input	Impact of crossing coupling	Efficiency	Stable performance	No. of Tx segment	Charging length ratio	Positioning
[9]	NSDS (S-S)	Yes	-	35%~85.3%	No	3	5.3	No
[10]	PTDS (LCC-S)	Yes	-	65%~84%	No	2	4.7	Additional sensors
[12]	PTDS (LCC-S)	-	Existing	80%~90%	Stable power	2	4.8	No
[13]	PTDS (LCC-S)	-	Existing	-	Stable power	4	4.5	No
[14]	PTDS (LCC-S)	-	Existing	89.7%	Stable efficiency and power	6	9	No
[15]	PTDS (LCC-S)	Yes	Eliminating	90.3%	Stable efficiency and power	7	3	No
[16]	PTDS (LCC-S)	Yes	Eliminating	90%	Stable efficiency and power	5	4	Integrated
[17]	NSDS (LCC-S)	-	Existing	79%~91%	Stable power	2	4.4	No
[18]	PTDS (LCC-S)	No	Eliminating	85%	Stable efficiency and power	2	4.4	No
[19]	STDS (LCC-S)	Yes	Eliminating	86.2%	Partial stage stabilized	2	4	Additional sensors
[20]	NSDS (LCC-S)	Yes	Eliminating	91.2%	Partial stage stabilized	3	5	No
This Work	**Pro_DS (CLL/S-S)**	**Yes**	**Eliminating**	**87%**	**Stable efficiency and power**	**2**	**9**	**Integrated**

parameters in Table IV are established and added in the prototype as shown in Fig. 27(a). Fig. 27(b) shows the efficiency and output voltage of the DWPT system when the Rx moves on the four Tx coils. The results show that both the efficiency and the output voltage of the designed DWPT system are reasonably stable during the movement, which is consistent with the system with two Tx coil segments. The stable charging area length produced by the DWPT system with four Tx coil segments is about 19.2 times the radius of the Rx coil. Thus, the proposed system with more Tx coil segments is effective.

C. System Comparison

Configuration of the proposed WPT system is compared with previous works reported in [9]–[20]. The common DWPT schemes with controlled segments can be divided into three categories. One is the normal segmented DWPT system (NSDS) with individual inverters [9], [16], [20], which includes an inverter and compensation network per Tx coil segment. The second is the parallel-Tx DWPT system (PTDS) with a switchable inverter, which includes a compensation network per Tx coil segment, and an inverter operating with multiple Tx coils in the PTDS [10]–[16], [18]. The last one is the series-Tx DWPT system (STDS) with switchable coils [19]. The system in [19] needs a variable capacitor matrix and many high-voltage switches to turn the Tx coils ON or OFF and tune the circuits. The DWPT scheme in [11] without any active switches reduces hardware cost, but the corresponding control flexibility also decreases.

Fig. 28 presents the number of components used in the NSDS and PTDS systems with the *LCC* compensation topology and the proposed DWPT system (Pro_DS), when two or four Tx coil segments are employed. As confirmed in Fig. 28, the proposed system saves inverter and compensation (capacitor when $n>1$, inductor when $n>2$) components compared with the two common DWPT schemes.

The performance comparison results with [9], [10], and [12]–[20] are listed in Table IX. Based on the proposed switching topology, ZPA input is achieved, and the impact of cross coupling is eliminated with fewer components. Differently, complex coil or inductor structures are designed to eliminate the cross coupling of adjacent Tx segments in [15], [16], and [20], and a capacitance matrix is employed in [19] to eliminate the impact. Furthermore, the individual Tx segment is extended for an enlarged stable and efficient coupling area to reduce the cost of hardware and control. The effective dynamic charging length produced by a Tx segment is four times the radius of the Rx coil, and the length produced by the DWPT system with two Tx coil segments is about nine times the radius of the Rx coil. The charging length ratio in Table IX is the ratio of the charging length to the Rx radius. Since there are two Rx coils in [10], half of the Rx length in the moving direction is recorded as the Rx radius. It can be seen that the proposed system employs fewer Tx segments to produce a longer charging area. Accordingly, the copper and control costs are lower. Meanwhile, the associated operating strategy and its system control with the embedded position detection configure the Tx segments based on the Rx position and stabilize the efficiency and output power. The efficiency of the proposed DWPT system is stable and close to that reported in the optimal-efficiency systems. Therefore, the construction of the proposed DWPT system is cost-effective, and the running cost of the system is acceptable/reasonable.

VI. CONCLUSION

In this article, a cost-effective DWPT system for dynamic charging of autonomous moving equipment with stable performance in terms of efficiency and output power is presented. The proposed system is based on the combination of a low-cost segmented DWPT configuration and its associated operating strategy. The *T*-series/series topology of the configuration tunes the circuits under different operating modes with fewer components. The Tx coil is designed for an extended stable and efficient coupling area, which along with the operating strategy, reduces the cost of segmented Tx for the required charging length. The proposed operating strategy also guarantees a stable dynamic efficiency without any degradation in all operating stages. The segmented Tx coils are configured/coordinated based on the system control that embeds position detection and power regulation capabilities. With the strategy and system control, stable dynamic charging performance in terms of efficiency and output power are realized. The low-cost configuration and its associated operating strategy, which includes the simplified tuning topology, extended Tx coil design, and integrated system control, make the proposed DWPT system cost-effective. Depending on a specific application and charging length, the proposed system can be flexibly deployed as follows.

1) If the required lateral misalignment tolerance, Rx coil size, or airgap distance changes according to the application conditions, the Tx and Rx coils can be redesigned based on the proposed coil design method in Section III-A.
2) If the required charging length is changed, the segmented Tx coils can be arranged based on the proposed DWPT scheme according to the length requirement.

REFERENCES

[1] Z. Zhang, H. Pang, A. Georgiadis, and C. Cecati, "Wireless power transfer—An overview," *IEEE Trans. Ind. Electron.*, vol. 66, no. 2, pp. 1044–1058, Feb. 2019.

[2] C. C. Mi, G. Buja, Y. C. Su, and C. T. Rim, "Modern advances in wireless power transfer systems for roadway powered electric vehicles," *IEEE Trans. Ind. Electron.*, vol. 63, no. 10, pp. 6533–6545, Oct. 2016.

[3] S. Hui, "Planar wireless charging technology for portable electronic products and Qi," *Proc. IEEE*, vol. 101, no. 6, pp. 1290–1301, Jun. 2013.

[4] G. Song, H. Wang, J. Zhang, and T. Meng, "Automatic docking system for recharging home surveillance robots," *IEEE Trans. Consum. Electron.*, vol. 57, no. 2, pp. 428–435, May 2011.

[5] H. Cai, G. Shao, J. Hu, Z. Wen, X. Wang, and J. Lyu, "Analysis of the main performance index and application status of inspection robot in substation," *Elect. Meas. Instrum.*, vol. 54, no. 14, pp. 117–123, Jul. 2017.

[6] A. Zaheer, G. A. Covic, and D. Kacprzak, "A bipolar pad in a 10-kHz 300-W distributed IPT system for AGV applications," *IEEE Trans. Ind. Electron.*, vol. 61, no. 7, pp. 3288–3301, Jul. 2014.

[7] S. Y. Choi, B. W. Gu, S. Y. Jeong, and C. T. Rim, "Advances in wireless power transfer systems for roadway-powered electric vehicles," *IEEE J. Emerg. Sel. Topics Power Electron.*, vol. 3, no. 1, pp. 18–36, Mar. 2015.

[8] J. M. Miller, P. T. Jones, J. Li, and O. C. Onar, "ORNL experience and challenges facing dynamic wireless power charging of EVs," *IEEE Circuits Syst. Mag.*, vol. 15, no. 2, pp. 40–53, May 2015.

[9] S. Huang, T. Lee, W. Li, and R. Chen, "Modular on-road AGV wireless charging systems via interoperable power adjustment," *IEEE Trans. Ind. Electron.*, vol. 66, no. 8, pp. 5918–5928, Aug. 2019.

[10] H. Liu *et al.*, "Dynamic wireless charging for inspection robots based on decentralized energy pickup structure," *IEEE Trans. Ind. Informat.*, vol. 14, no. 4, pp. 1786–1797, Apr. 2018.

[11] S. Y. Jeong, J. H. Park, G. P. Hong, and C. T. Rim, "Autotuning control system by variation of self-inductance for dynamic wireless EV charging with small air gap," *IEEE Trans. Power Electron.*, vol. 34, no. 6, pp. 5165–5174, Jun. 2019.

[12] Y. Wang, F. Lin, Z. Yang, P. Cai, and Z. Liu, "Coils layout optimization of dynamic wireless power transfer system to realize output voltage stable," in *Proc. Int. Power Electron. Conf. (IPEC-Niigata-ECCE Asia)*, 2018, pp. 3495–3500.

[13] A. Mukhatov, M. Bagheri, P. Dehghanian, V. Carabias, and G. B. Gharehpetian, "Reduction of output power pulsations for electric vehicles by changing distances between transmitter coils," in *Proc.7th Int. Conf. Renewable Energy Res. Appl.*, 2018, pp. 307–312.

[14] F. Lu, H. Zhang, H. Hofmann, and C. Mi, "A dynamic charging system with reduced output power pulsation for electric vehicles," *IEEE Trans. Ind. Electron.*, vol. 63, no. 10, pp. 6580–6590, Oct. 2016.

[15] Y. Li *et al.*, "A new coil structure and its optimization design with constant output voltage and constant output current for electric vehicle dynamic wireless charging," *IEEE Trans. Ind. Informat.*, vol. 15, no. 9, pp. 5244–5256, Sep. 2019.

[16] X. Li, J. Hu, H. Wang, X. Dai, and Y. Sun, "A new coupling structure and position detection method for segmented control dynamic wireless power transfer systems," *IEEE Trans. Power Electron.*, vol. 35, no. 7, pp. 6741–6745, Jul. 2020.

[17] Q. Zhu, Y. Guo, S. Li, L. Wang, and C. Liao, "Segmental switching strategy with zero output pulsation for dynamic EV wireless charging system," *IET Power Electron.*, vol. 12, no. 6, pp. 1563–1570, Jun. 2019.

[18] S. Li, L. Wang, Y. Guo, C. Tao, and L. Ji, "Power stabilization with double transmitting coils and T-type compensation network for dynamic wireless charging of EV," *IEEE J. Emerg. Sel. Topics Power Electron.*, vol. 8, no. 2, pp. 1801–1812, Jun. 2020.

[19] H. Liu, L. Tan, X. Huang, M. Zhang, Z. Zhang, and J. Li, "Power stabilization based on switching control of segmented transmitting coils for multi loads in static-dynamic hybrid wireless charging system at traffic lights," *Energies*, vol. 12, no. 4, Feb. 2019, Art. no. 607.

[20] F. Farajizadeh, D. M. Vilathgamuwa, D. Jovanovic, P. Jayathurathnage, G. Ledwich, and U. Madawala, "Expandable N-legged converter to drive closely spaced multitransmitter wireless power transfer systems for dynamic charging," *IEEE Trans. Power Electron.*, vol. 35, no. 4, pp. 3794–3806, Apr. 2020.

[21] C. Cai, J. Wang, H. Nie, P. Zhang, Z. Lin, and Y. Zhou, "Effective-configuration WPT systems for drones charging area extension featuring quasi-uniform magnetic coupling," *IEEE Trans. Transp. Electrific.*, vol. 6, no. 3, pp. 920–934, Sep. 2020.

[22] X. Dai, J. Jiang, and J. Wu, "Charging area determining and power enhancement method for multiexcitation unit configuration of wirelessly dynamic charging EV system," *IEEE Trans. Ind. Electron.*, vol. 66, no. 5, pp. 4086–4096, May 2019.

[23] X. Liu and S. Y. Hui, "Optimal design of a hybrid winding structure for planar contactless battery charging platform," *IEEE Trans. Power Electron.*, vol. 23, no. 1, pp. 455–463, Jan. 2008.

[24] J. Kim, D. H. Kim, and Y. J. Park, "Free-positioning wireless power transfer to multiple devices using a planar transmitting coil and switchable impedance matching networks," *IEEE Trans. Microw. Theory Techn.*, vol. 64, no. 11, pp. 3714–3722, Nov. 2016.

[25] S. Wang, Z. Hu, C. Rong, C. Lu, J. Chen, and M. Liu, "Planar multiple-antiparallel square transmitter for position-insensitive wireless power transfer," *IEEE Antennas Wireless Propag. Lett.*, vol. 17, pp. 188–192, 2018.

[26] Z. Zhang, H. Pang, C. H. T. Lee, X. Xu, X. Wei, and J. Wang, "Comparative analysis and optimization of dynamic charging coils for roadway-powered electric vehicles," *IEEE Trans. Magn.*, vol. 53, no. 11, Nov. 2017, Art. no. 9402106.

[27] H. Z. Z. Beh, G. A. Covic, and J. T. Boys, "Wireless fleet charging system for electric bicycles," *IEEE J. Emerg. Sel. Topics Power Electron.*, vol. 3, no. 1, pp. 75–86, Mar. 2015.

[28] W. Zhang and C. C. Mi, "Compensation topologies of high-power wireless power transfer systems," *IEEE Trans. Veh. Technol.*, vol. 65, no. 6, pp. 4768–4778, Jun. 2016.

[29] A. Dalal, T. P. E. Reena Joy, and P. Kumar, "Mutual inductance computation method for coils of different geometries and misalignments," in *Proc. IEEE Power Energy Soc. Gen. Meeting*, Denver, CO, USA, 2015, pp. 1–5.

[30] B. Zhang, Q. Chen, G. Ke, L. Xu, X. Ren, and Z. Zhang, "Coil positioning based on DC pre-excitation and magnetic sensing for wireless electric vehicle charging," *IEEE Trans. Ind. Electron.*, vol. 68, no. 5, pp. 3820–3830, May 2021.

[31] F. W. Grover, *Inductance Calculations*. New York, NY, USA: Van Nostrand, 1946.

[32] R. R. Harrison, "Designing efficient inductive power links for implantable devices," in *Proc. IEEE Int. Symp. Circuits Syst.*, New Orleans, LA, USA, 2007, pp. 2080–2083.

[33] M. Leibl, O. Knecht, and J. W. Kolar, "Inductive power transfer efficiency limit of a flat half-filled disc coil pair," *IEEE Trans. Power Electron.*, vol. 33, no. 11, pp. 9154–9162, Nov. 2018.

[34] F. Lu, H. Zhang, H. Hofmann, W. Su, and C. C. Mi, “A dual-coupled LCC-compensated IPT system with a compact magnetic coupler,” *IEEE Trans. Power Electron.*, vol. 33, no. 7, pp. 6391–6402, Jul. 2018.

[35] P. Zhang, M. Saeedifard, O. C. Onar, Q. Yang, and C. Cai, “A field enhancement integration design featuring misalignment tolerance for wireless EV charging using LCL topology,” *IEEE Trans. Power Electron.*, vol. 36, no. 4, pp. 3852–3867, Apr. 2021.

[36] F. Lu, H. Hofmann, J. Deng, and C. Mi, “Output power and efficiency sensitivity to circuit parameter variations in double-sided LCC-compensated wireless power transfer system,” in *Proc. IEEE Appl. Power Electron. Conf. Expo.*, 2015, pp. 597–601.

[37] Q. Bo, Y. Zhang, Y. Guo, L. Wang, Z. Liu, and S. Li, “Sensitivity analysis to parameter variations in LCC-S compensated inductive power transfer systems,” in *Proc. IEEE PELS Workshop Emerg. Technol., Wireless Power Transf.*, 2020, pp. 233–237.

[38] G. Lovison, T. Imura, and Y. Hori, “Secondary-side-only simultaneous power and efficiency control by online mutual inductance estimation for dynamic wireless power transfer,” in *Proc. 42nd Annu. Conf. IEEE Ind. Electron. Soc.*, Oct. 2016, pp. 4553–4558.

[39] Y. Su, L. Chen, X. Wu, A. P. Hu, C. Tang, and X. Dai, “Load and mutual inductance identification from the primary side of inductive power transfer system with parallel-tuned secondary power pickup,” *IEEE Trans. Power Electron.*, vol. 33, no. 11, pp. 9952–9962, Nov. 2018.

[40] Y. Yang, S. C. Tan, and S. Y. R. Hui, “Fast hardware approach to determining mutual coupling of series-series-compensated wireless power transfer systems with active rectifiers,” *IEEE Trans. Power Electron.*, vol. 35, no. 10, pp. 11026–11038, Oct. 2020.

Changsong Cai (Member, IEEE) received the Ph.D. degree in electrical engineering from Wuhan University, Wuhan, China, in 2020.

He is currently a Postdoctoral Research Fellow with the School of Electrical Engineering and Automation, Wuhan University. From 2019 to 2020, he was a Visiting Researcher with the School of Electrical and Computer Engineering, Georgia Institute of Technology, Atlanta, GA, USA. His research interests include engineering electromagnetism and power electronics, and the research mainly involves wireless power transfer and its industrial applications.

Maryam Saeedifard (Fellow, IEEE) received the Ph.D. degree in electrical engineering from the University of Toronto, Toronto, ON, Canada, in 2008.

She is currently as Associate Professor with the School of Electrical and Computer Engineering, Georgia Institute of Technology, Atlanta, GA, USA. Prior to joining Georgia Institute of Technology, she was an Assistant Professor with the School of Electrical and Computer Engineering, Purdue University, West Lafayette, IN, USA. Her research interests include power electronics and applications of power electronics in power systems.

Junhua Wang (Member, IEEE) was born in Shandong, China, in 1981. He received the Ph.D. degree from Hong Kong Polytechnic University, Hong Kong, in 2012.

He is currently a Professor with the School of Electrical Engineering and Automation, Wuhan University, Wuhan, China. In 2012, he joined Carnegie Mellon University, Pittsburgh, PA, USA, as a Postdoctoral Researcher, and then worked as a Research Fellow with GATE Center for Electric Drive Transportation, University of Michigan-Dearborn, Dearborn, MI, USA. His research interests include wireless transfer technology based on magnetic resonance, applied electromagnetics, and system equipment for power transmission and distribution.

Pengcheng Zhang (Member, IEEE) received the Ph.D degree in electrical engineering from the Hebei University of Technology, Tianjin, China, in 2021.

From November 2017 to December 2019, he was a Visiting Researcher with the School of Electrical and Computer Engineering, Georgia Institute of Technology, Atlanta, GA, USA. He is currently a Postdoctoral Researcher with the Department of Electrical Engineering, Tsinghua University, Beijing, China. His research interests include engineering electromagnetism, wireless power transfer, and its industrial applications.

Jiansong Zhao was born in China, in 1996. He received the B.S. degree in electrical engineering and automation from the Huazhong University of Science and Technology, Wuhan, China, in 2019. He is currenty working toward the M.S. degree in electrical engineering with Wuhan University, Wuhan, China.

His research interests include wireless power transfer and its industrial applications.

Yunshan Hong was born in Hubei, China, in 1998. She received the B.S. degree in 2020 from Wuhan University, Wuhan, China, where she is currently working toward the M.S. degree in electrical engineering with the School of Electrical Engineering and Automation.

Her current research interests include wireless transfer technology based on magnetic resonance.